Digital Image Acquisition

2

Abstract

Medical images are pictures of distributions of physical attributes captured by an image acquisition system. Most of today's images are digital. They may be postprocessed for analysis by a computer-assisted method.

Medical images come in one of two varieties: Projection images project a physical parameter in the human body on a 2D image, while slice images produce a one-to-one mapping of the measured value. Medical images may show anatomy including the pathological variation of anatomy if the measured value is related to it or physiology when the distribution of substances is traced.

X-ray imaging, CT, MRI, nuclear imaging, ultrasound imaging, photography, and microscopic images will be discussed in this chapter. The discussion focuses on the relationship between the imaged physical entity and the information shown in the image, as well as on reconstruction methods and the resulting artefacts.

Concepts, notions and definitions introduced in this chapter

- *Imaging techniques*: x ray, fluoroscopy and angiography, DSA, x-ray CT, CT angiography, MR imaging, MR angiography, functional MRI, perfusion MRI, diffusion MRI, scintigraphy, SPECT, PET
- *Reconstruction techniques*: filtered backprojection, algebraic reconstruction, EM algorithms
- *Image artefacts*: noise, motion artefacts, partial volume effect, MR-specific artefacts, ultrasound-specific artefacts

A major difference between most digital medical images and pictures acquired from photography is that the depicted physical parameters in medical images are usually inaccessible for inspection (see Fig. 2.1). Features or quantities determined by computer-assisted analysis cannot easily be compared with true features or quantities. It would be, e.g., infeasible to open the human body to verify whether a tumor

K.D. Toennies, *Guide to Medical Image Analysis*,
Advances in Computer Vision and Pattern Recognition,
DOI 10.1007/978-1-4471-2751-2_2,

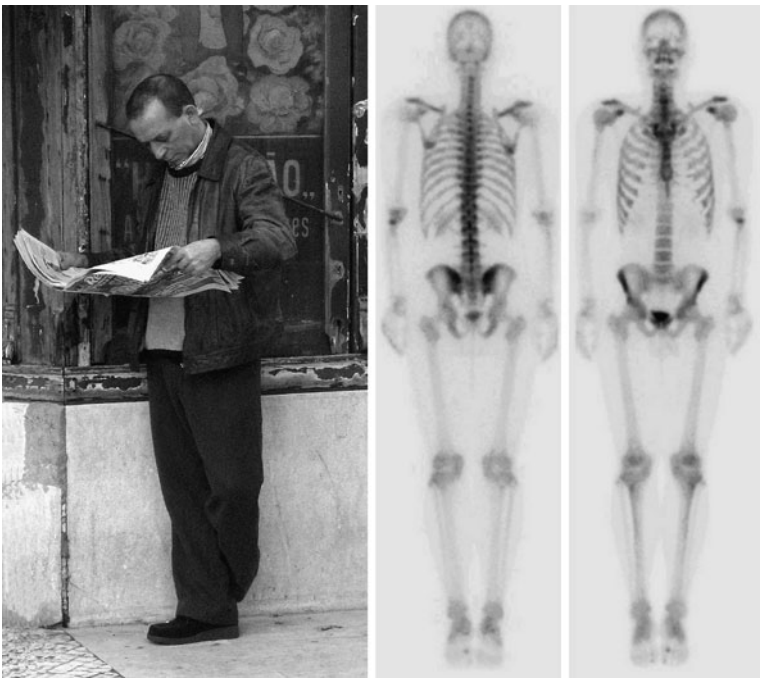

Fig. 2.1 Information from a photography is quite different from that of a medical image (in this case a bone scintigraphy, published under Creative Commons license). While the human depicted in the photo looks familiar, interpretation of the *image on the right* requires expertise with respect to the meaning of the intensities. On the other hand, specific domain knowledge exists as to how to interpret image intensity in the scintigraphy and the image is acquired in a way that makes analysis as easy as possible, all of which cannot be said about the *picture on the left*. Obviously, the kind of task for computer-based image analysis is different for these two pictures

volume measured in a sequence of CT images in some posttreatment confirmation scan corresponds to the true volume.

Fortunately, the physical property depicted, its diagnostic value, and possible artefacts are usually well known. Furthermore, the imaging technique has been chosen on purpose because it is known to produce images that depict diagnostically relevant information. The development of efficient analysis techniques often uses this knowledge as part of the domain knowledge to make up for the inaccessibility of the measured property.

A physical property measured by an imaging device and presented as a picture must meet three conditions to be useful. It has to penetrate the human body, it must not unduly interfere with it, and it must be meaningful for answering some medically relevant question.

With respect to digital imaging, four major[1] and several minor imaging techniques meet these requirements. The major techniques are as follows.

- *X-ray imaging* measures the absorption of short wave electromagnetic waves, which is known to vary between different tissues.
- *Magnetic resonance imaging* measures the density and molecular binding of selected atoms (most notably hydrogen which is abundant in the human body), which varies with tissue type, molecular composition, and functional status.
- *Ultrasound imaging* captures reflections at the boundaries between and within tissues with different acoustic impedance.
- *Nuclear imaging* measures the distribution of radioactive tracer material administered to the subject through the blood flow. It measures function in the human body.

Other imaging techniques include *EEG* and *MEG imaging*, *microscopy*, and *photography*. All the techniques have in common that an approximate mapping is known between the diagnostic question, which was the reason for making the image and the measurement value that is depicted. This can be very helpful when selecting an analysis technique. If, for instance, bones need to be detected in an x-ray CT slice, a good first guess would be to select a thresholding technique with a high threshold because it is known that x-ray attenuation in bone is higher than in soft tissues and fluids.

Many of the imaging techniques come in two varieties: *Projection images* show a projection of the 3D human body onto a 2D plane and *slice images* show a distribution of the measurement value in a 2D slice through the human body. Slice images may be stacked to form a volume. Digitized images consist of a finite number of image elements. Elements of a 2D picture are called *pixels* (picture elements) and elements of stacked 2D slices are called *voxels* (volume elements). We will call pixels or voxels *scene elements* if the dimension of the scene is not known or not important.

2D and 3D images may have an additional time dimension if the variation along the time axis provides additional diagnostic information (e.g., if normally and abnormally beating hearts are compared). Slice images are usually reconstructed from some kind of projection. Reconstruction may cause additional artefacts.

The chapter provides an overview on image acquisition systems for digital images in medicine. Emphasis is put on the semantics of the image and on system-specific artefacts. A more detailed look at the imaging techniques and the reconstruction of medical images is provided by specialized literature such as Prince and Links (2005) or the text of Bushberg et al. (2002) (the latter is more directed toward radiology residents). Imaging techniques in this chapter are listed by the kind of entity that is measured.

[1] Imaging techniques are ordered by importance with respect to digital imaging and digital image analysis. Orders of importance with respect to relevance to diagnosis or with respect to frequency of examination are different, of course.

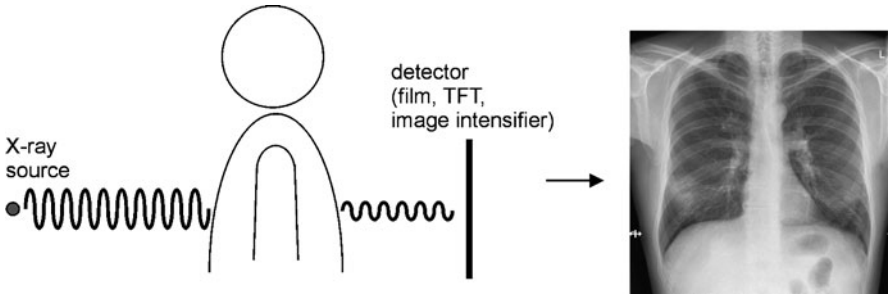

Fig. 2.2 X-rays penetrate the human body and produce an image that shows the integral of tissue-specific absorption along a path from the X-ray source to a detector

2.1 X-Ray Imaging

X rays were discovered in 1895 by Wilhelm Röntgen.[2] He noticed an unknown kind of ray emitted by a cathode ray tube (CRT) that easily penetrated paper, aluminum, and many other materials, but not a lead plate. He also found that this kind of ray is not reflected, refracted, diffracted, or deflected by electrical fields. He discovered that the rays blackened film so that photographic images could be produced. Röntgen called this unknown type of radiation *x rays*.

A material-specific amount of the energy of an x ray is attenuated when penetrating a material. For the first time in history, a technique allowed noninvasive insight into the human body (see Fig. 2.2).

The harmful aspects of x rays were not known in the early years. It was employed for all kinds of purposes without balancing the potential information gain through imaging against the harmfulness of exposure to radiation. For instance, until the 1960s, some shoe stores offered a service by which customer's feet wearing shoes to be fitted were x rayed. Few, if any, precautions were taken to secure operators of x-ray machines from harmful exposure.

2.1.1 Generation, Attenuation, and Detection of X Rays

X rays are electromagnetic waves with a wavelength above the visible spectrum. Electromagnetic radiation has the characteristics of waves, but is actually traveling as clusters of energy called *photons* with a given wavelength. Electromagnetic waves do not need a carrier such as sound waves and travel at the speed of light c. Their wavelength λ and frequency f are related by

$$c = \lambda f. \tag{2.1}$$

[2]Carl Wilhelm Röntgen was Professor for physics at the Julius-Maximilian-Universität Würzburg, when he discovered x rays in his experiments with the cathode ray tube in 1895. He received the Nobel price in Physics for his discovery.

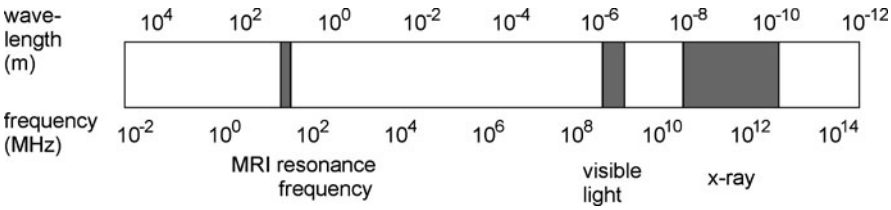

Fig. 2.3 The spectrum of diagnostic X-ray is above the spectrum of visible light in the range of 0.01 to 15 nm (10^{-11} to 1.5×10^{-8} m)

The energy of a photon measured in electron volts (eV) is the energy that a single electron acquires when moving through a potential of 1 V. The energy of a photon is characterized by its wavelength. It is given by

$$e = 1.24/\lambda \tag{2.2}$$

if the unit of measurement is a kilo electron volt (keV) and the wavelength is measured in nanometers (nm).

The wavelength of an electromagnetic wave corresponds to its energy. Examples for electromagnetic waves, in the order of increasing energy, are radio waves (being used for magnetic resonance imaging), visible light, and x rays or gamma rays (see Fig. 2.3). The difference between x rays and gamma rays is not their wavelength, but the fact that gamma rays are created in the nucleus of an atom while x rays are not. The energy of x-ray photons is sufficient to release electrons from an atom, a process which is called *ionizing radiation*.

X rays are characterized by their *exposure*, i.e., the amount of charge per volume of air, which is measured in röntgen (R). Exposure measures the energy of the radiation source, but it does not describe how much of the radiation is absorbed by a body under radiation. Absorption per unit mass is called *dose* and it is measured in radiation absorbed dose (rad) or gray (Gy) with 1 Gy = 100 rad. The ratio between exposure and dose varies with the x-ray energy and is often called the f-factor. The f-factor at low exposure for hard tissues such as bone is much higher than for soft tissues and water. Hence, bone at low doses absorbs a significantly higher amount of radiation than soft tissues.

2.1.1.1 X-Ray Generation

Understanding the different types of x rays requires some understanding about their generation. Electrons in an atom are organized in shells around the nucleus. Since the negatively charged electrons are attracted to the protons in the nucleus, the innermost shell contains electrons with the lowest energy. Energy is needed for moving an electron from an inner shell to an outer shell, which is equivalent to the difference between energy levels of the two shells. If an electron is released from a shell, the required energy amounts to the difference between its current energy level and the level of the outermost shell plus the energy to remove an electron from the outermost shell. Electrons on the outermost shell are thus the easiest to remove and are called *valence electrons*.

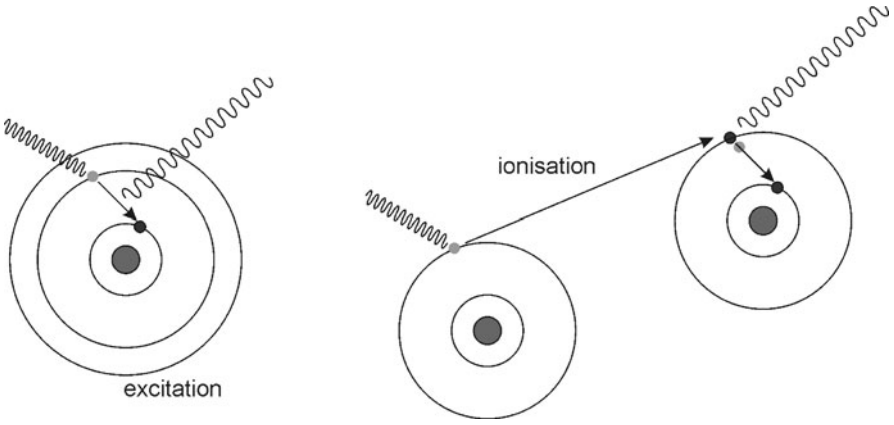

Fig. 2.4 X-ray generation by excitation and ionization. In excitation, external energy pushes an electron from an outer shell to an inner shell. Excess energy is released as x rays. The ionization process is similar, except for the fact that excitation happens indirectly by an electron that is released from an outer shell of a different atom

X rays are generated as excess energy from electrons in the material of a *cathode ray tube* (CRT)[3] when heating the cathode. Energy from heating causes electrons to be released from the cathode and accelerated toward the anode. In the anode, electrons lose their kinetic energy by excitation, ionization, and radiation. *Excitation* and *ionization* cause electrons of the anode material to move from an outer shell to an inner shell (see Fig. 2.4). For excitation, this happens directly, whereas ionization causes the electrons of an outer shell to be released, which then excites the electrons of another atom. The excess energy being released as x rays depends on the energy difference between the outer and the inner shells. Hence, the radiation from this process is monochrome. This kind of x ray is called *characteristic* or *monochrome* x-ray radiation.[4]

Most of the x-ray radiation, however, is *polychrome*. An incident electron is slowed down by passing the nucleus of an atom. Slowing down means that the frequency of the electron changes. The excess energy is emitted as a photon. Its amount depends on how close the incident electron passes to the nucleus. All its energy is released as x rays if it annihilates in the nucleus. If it passes the nucleus, more energy is released for an inner shell passage than for an outer shell passage. This type of radiation is called *bremsstrahlung* and it is inherently polychrome (see Fig. 2.5).

[3]The material for anode and cathode is usually Tungsten (also called Wolfram), a chemical element belonging to the metals with the highest melting point of all metals. In CRTs for mammography, another metal, Molybdenum, is used.

[4]The detection of characteristic x ray radiation by Charles G. Barkla in 1905 resulted in another Nobel price in Physics presented to its discoverer in 1917.

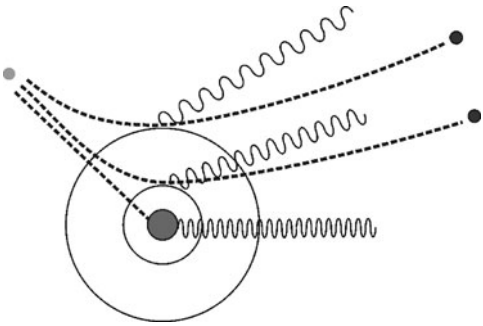

Fig. 2.5 Polychrome radiation is a result of a passage of an electron. The frequency of the released radiation depends on the extent to which the electron loses its energy

The likelihood of passing an atom at a given distance increases with the distance to the nucleus because the surface of a sphere of a given radius increases with the radius. Thus, the spectrum of the bremsstrahlung of a cathode ray tube should roughly be of a triangular shape. However, the surrounding glass of the tube filters some of the low-energy radiation. Hence, the actual curve is zero at low energy levels, then increases to some maximum at intermediate energy levels and finally decreases to zero at the maximum energy (which is the maximum energy of electrons incident on the anode of the tube). The complete spectrum of a typical x-ray tube is a combination of monochrome and polychrome radiation, where some spikes indicate various characteristic radiation energy levels in the otherwise smooth curve.

X-ray tubes are characterized by the total amount of energy that is emitted as x rays and the quality of the radiation. A high-quality tube has a higher ratio of high-energy radiation and of monochrome radiation. High-quality radiation imposes a lower dose on the patient and generally produces better images.

The quantity and quality of x-ray radiation depend on a number of characteristics of the tube (such as the anode material) and on the parameters to be selected by the operators (such as the potential between cathode and anode, voltage, and exposure time).

The quality of the emitted x rays can be enhanced by a filtering process called *beam hardening*. The glass surrounding the tube already filters some of the low-energy rays of the bremsstrahlung. It reduces the total energy of the emitted x rays, but shifts the spectrum toward the high-quality range. The emitted frequency range can be further improved by the additional filtering of low-frequency components. The amplitude of monochrome radiation is usually higher than that of bremsstrahlung. Beam hardening may thus be used for an overall reduction of x-ray radiation enhancing monochrome radiation in the spectrum as well.

2.1.1.2 X-Ray Attenuation

When x rays enter the human body, four types of attenuation can happen: Raleigh, scatter, Compton scatter, photoelectric absorption, and pair production (see Fig. 2.6). Of these, Compton scatter and photoelectric absorption are the main factors for image generation from medium-range energy x-ray imaging such as that used in diagnostic imaging.

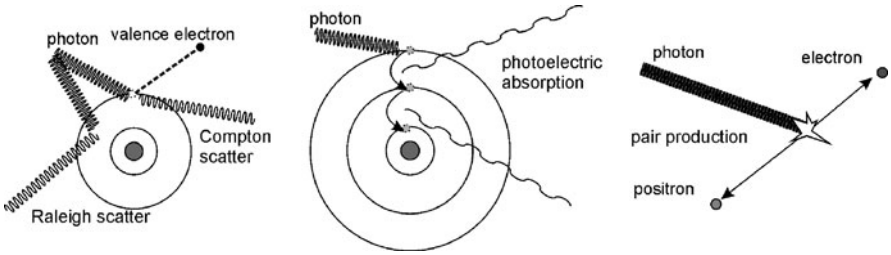

Fig. 2.6 Four kinds of X-ray attenuation exist. Raleigh and Compton scatter causes noise in the image since the scatter direction is random. Photo-electric absorption produces the X-ray image, since the released energy is too low to be detected. The energy levels used in X-ray imaging do not produce pair production

Raleigh scatter mainly happens in low-energy imaging such as mammography. A photon causing Raleigh scatter loses its energy by exciting the whole atom, which immediately releases a photon with almost the same energy, although usually scattered in a different direction.

A photon causing *Compton scatter* will release a valence electron from its shell. It will lose as much energy as was necessary for the release. Scattered photons will change their direction.

Scatter, be it Raleigh scatter or Compton scatter, increases noise and reduces contrast in an image. Noise stems from the randomness of scattering and the random change of direction for scattered photons. Contrast is reduced because scattered photons reaching the receptor do not carry position information of the locus of scattering, thus only increasing the overall brightness in the image.

Photoelectric absorption is the main contributor to imaging even though absorption in diagnostic x rays happens less often than Compton scattering. A photon releases its energy through photoelectric absorption by removing one of the electrons of the inner shells. The photon loses its energy completely. The released electron leaves a vacancy in the shell that is filled by an electron of one of the outer shells. This initiates a cascade of filling in the vacancies from the outer shells. The energy gain from each transition is released as characteristic radiation. The characteristic radiation caused by this process has a much lower energy than that of the incident photon. Hence, it is absorbed by the surrounding atoms and does not contribute to the degradation of the image. Absorption is the cause of a meaningful image, but it also increases the radiation dose absorbed by the tissue.

The probability of absorption increases with atomic number (e.g., the calcium in bone absorbs more than the hydrogen of the cerebrospinal fluid) and decreases with beam energy. Absorption increases dramatically when the photon energy equals the binding energy of an inner electron. This value is called the *absorption edge* and its existence is exploited by *contrast agents*. Contrast agents such as iodine and barium have a high atomic number and an absorption edge in the range of diagnostic x rays (33 and 37 keV). The high atomic number already increases the probability of absorption. Energy in the range of the absorption edge of the radiation spectrum will be further reduced.

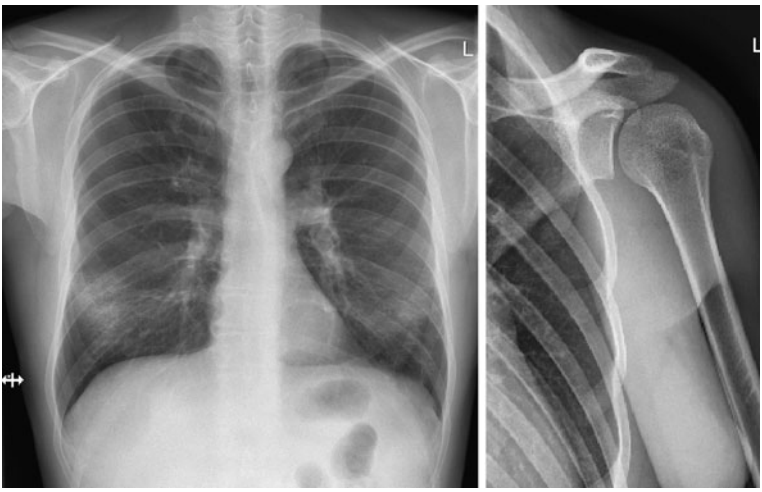

Fig. 2.7 Two radiographs (with kind permission from Siemens Sector Healthcare, Erlangen, Germany). Bone structures in the two images are clearly visible. Differentiating between different soft tissues is more difficult as is the depth order of the projected structures

Pair production, the last of the four effects, happens only if the energy exceeds 1022 keV, which is beyond the usual diagnostic range for x-ray imaging. In pair production, a photon annihilates and produces an electron–positron pair. The positron and electron are sent in opposite directions. Although this is not relevant for x-ray imaging, it should be noted that the opposite process (i.e., the annihilation of a positron when merging with an electron producing two photons with 511 keV) is used for positron emission tomography (PET), an imaging technique that is described later in this chapter.

2.1.2 X-Ray Imaging

X-ray imaging uses the dependency of photoelectric absorption on the atomic number for producing a diagnostically meaningful image (see Fig. 2.7 for examples). Being the oldest technique, a vast number of different imaging methods evolved from the original method presented by C.W. Röntgen. In this section we will only touch on the subject to give an impression of how the images are created and what kind of different x-ray imaging techniques exist. A more detailed treatment can be found in Bushberg et al. (2002) and Prince and Links (2005). Much of this section has been taken from there and from the AAPN/RSNA Physics Tutorial for Residents that appeared in various issues of the Radiographics journal (McCollough 1997; Bushberg 1998; McKetty 1998; Pooley et al. 2001; Wang and Blackburn 2000).

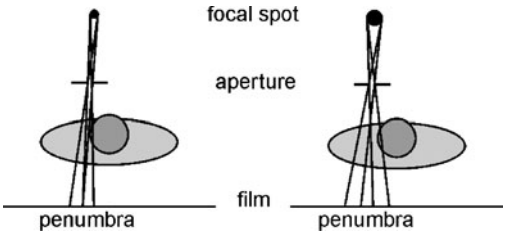

Fig. 2.8 Different sizes of the focal spot cause different blurring even if the aperture is the same

Diagnostic equipment for x-ray imaging consists at least of a cathode ray tube emitting x rays and a receptor with the patient placed between the emitter and receptor. The receptor may be film, an image intensifier, or a flat panel detector with the latter two producing digital images.

If the x-ray tube is assumed to be a point source for x rays and the receptor is planar, the image intensity at every location of the receptor will be proportional to the attenuation along a ray from the x-ray tube to the receptor. The measured intensity for a monochromatic beam at a location (x, y) on the receptor is then

$$I_{\text{out}} = I_{\text{in}} \cdot \exp\left(- \int_{s_0}^{s_1} \mu(s)\, ds \right), \tag{2.3}$$

where I_{in} is the incident intensity of x rays when entering the body, s is a ray from the x-ray source to (x, y) on the image plane, s_1 is the point where the ray enters the body, and s_2 is the point where it exits the body. The function $\mu(s)$ is the *attenuation*. Attenuation, as pointed out in the previous section, is mainly caused by Compton scatter and photoelectric absorption and to a small extent by Raleigh scatter. The intensity at some location (x, y) is given by x-ray attenuation plus intensity due to scattered photons. If scattered photons are assumed to be distributed evenly over the image, they increase the brightness in the image by a noise component thus reducing contrast.

The imaging process described above is idealized in that it assumes that the x-ray source is a point source. In reality, the *focal spot* of an x-ray source covers a finite area leading to a loss of resolution due to penumbrae. Its extent depends on the distances between the source, object, and receptor, as well as on the diameter of the focal spot (see Fig. 2.8). Regular x-ray CRTs have a focal spot with a diameter of 1 mm, fine focus CRTs have one with a 0.5-mm diameter and microfocus CRT has a 0.2-mm diameter focal spot.

Integrated attenuation along s of polychromatic x rays is different to the monochromatic case described above since low-energy radiation is absorbed earlier than high-energy radiation. Placing the patient between the source and receptor causes additional beam hardening. Continuous beam hardening of an x ray traveling through the body has the effect that attenuation changes depending on the distance traveled in the body. This makes the image content dependent on patient positioning. It also causes some of the low-energy radiation to be absorbed by the patient without having an impact on the images and unnecessarily increases the dose. Prior beam hardening by filtering lessens these unwanted effects.

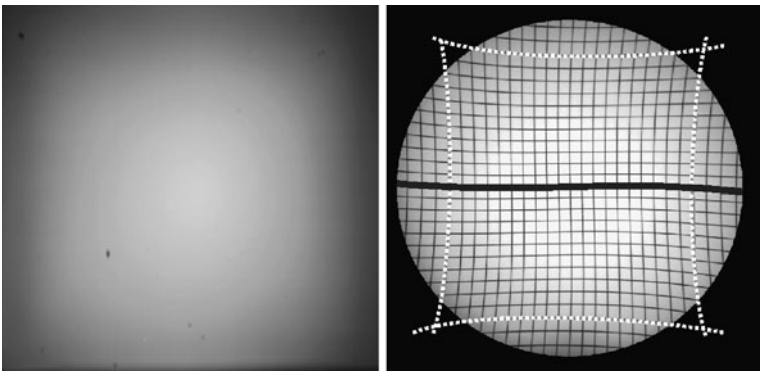

Fig. 2.9 Vignetting causes shading in an image as it can be seen in the picture of homogeneous *material on the left*. The location dependent magnification by a pincushion distortion of an image intensifier is seen on the test pattern of equal-sized *squares on the right* (*dashed lines*). This image also shows the much less prominent deformation due to the earth magnetic field

Of the three types of receptors *analogue film* is the oldest and still the most widespread. Film may be digitized, but receptors such as image intensifiers and flat panel detectors are preferred if computer-assisted postprocessing is desired.

An *image intensifier* produces a visible image from x rays in a similar fashion than a conventional CRT. X rays are turned into visible light on a phosphor screen in a vacuum tube, which is then converted into electrons by a photocathode. The electrons are focused and accelerated—this is the enhancement step—toward the anode and cast onto the output phosphor producing the intensified image. Enhancement through an image intensifier increases the brightness at the output phosphor more than 1000 times with respect to the very weak signal at the input phosphor.

The image intensifier was originally invented for creating a visible signal without the need to use and develop film. It has the additional advantage of enabling the transmittance of the electronic signal and its digitization through an A/D converter.

Images from an image intensifier suffer from a number of artefacts of which the following three are relevant for postprocessing (see Fig. 2.9).

- *Vignetting* is caused by the angle at which rays fall onto the input screen. The angle is perpendicular to the image screen in the center. In this case, the incident x-ray energy is distributed over the smallest possible area. The intensity (i.e., the energy per unit area) is maximal. The angle decreases with the distance to the center, causing the incident x-ray energy to be distributed over a larger area. Hence, the intensity decreases with the distance to the center.
- *Pincushion distortion* is caused by the curvedness of the input screen and results in magnification. Magnification increases with the deviation of the input surface from a tangent plane to the center of the screen.
- The *S-distortion* is caused by external electromagnetic fields that influence the course of the electron beam between the input and output phosphor.

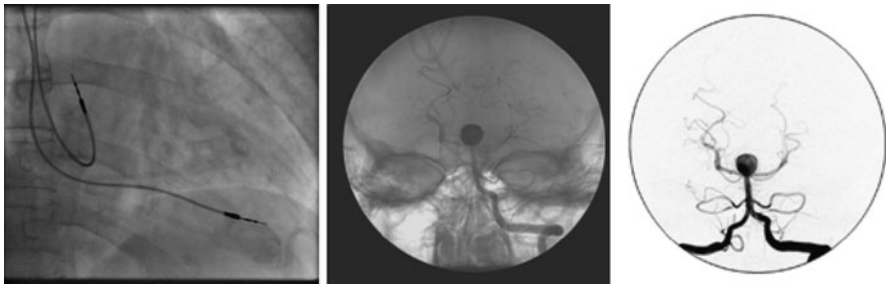

(a) (b) (c)

Fig. 2.10 (**a**) Fluoroscopy guiding pacemaker implanting (from knol.google.com/k/pacemakers, published under Creative Commons license). (**b**) Angiogram of cranial vessels showing an aneurysm (the eye sockets and parts of the skull are visible as well and hide some of the small vessels), (**c**) Digital subtraction angiogram of (**b**)

A completely digital receptor for x rays is the TFT *flat panel detector* that has been developed in recent years. A flat panel detector combines a flat panel scintillator, which turns x rays into visible light with a detector that transforms the light into an analogue electric signal, which then may be digitized. Several studies established the adequateness of using a flat panel detector in diagnostic imaging with the added advantage of lower doses necessary for imaging (e.g., Bacher et al. 2003; Fink et al. 2002; Garmer et al. 2000).

The *blackening curve*, which measures the dependency of incident radiation on the receptor and intensity of the resulting images, has a larger interval of linear increase for flat panel detectors and image intensifiers than for film. This decreases the likelihood of an accidental overexposure or underexposure. The spatial resolution in digital radiography is still lower than that of film. However, recent advances in TFT detector design have pushed the limits of achievable resolution into the range of film (about 4000×4000 pixels).

An advantage of digital radiography using either a TFT detector or an image intensifier is that the operator may choose the spatial resolution. If imaging at a lower resolution is sufficient for some diagnostic purpose, this can be achieved by analogue or digital integration over several pixels of the image. Since integration reduces noise, the signal-to-noise ratio increases without having to increase the exposure and, consequently, the dose.

2.1.3 Fluoroscopy and Angiography

Fluoroscopy is a specific kind of x-ray imaging to visualizes moving or changing objects in the human body (see Fig. 2.10a). Examples for using diagnostic fluoroscopy are as follows:

- to follow the heartbeat for detecting abnormal behavior,

- to follow the course of a contrast agent through the colon to detect potential abnormalities such as a tumor,
- to image cardiac or cerebral blood flow by using a contrast agent.

The technique received its name because x rays are turned into visible light using a fluorescent screen. Early fluoroscopy systems placed the screen directly behind the x-ray tube and the patient. The physician was sitting in front of the screen. Fluorescence from the x rays is very weak so that the introduction of the image intensifier made fluoroscopic imaging a much more viable tool.

Most of today's fluoroscopic imaging devices produce digital images and enable the creation of x-ray films as well. Fluoroscopic imaging devices are not necessarily static. When mounted on a C-arm, they can be rotated around the patient for producing projections along arbitrary directions. Fluoroscopic imaging is used for diagnosis and supports surgical interventions. It is an attractive imaging technique for the latter usage because images can be produced during the intervention.

Fluoroscopic imaging of the vascular system using a contrast agent is called *angiography* (see Fig. 2.10b). The contrast agent is applied by a catheter being guided to the location to be imaged (e.g., the brain or the heart wall). Imaging cerebral or cardiovascular flow supports the diagnosis of arteriosclerosis, arterio-venous malformations (AVMs), and so on. Angiographic images show anatomy of the human body with the blood vessels enhanced through the contrast agent. Angiographic images can be acquired in real-time and can be used to guide a surgical intervention (see Fig. 2.11 for a modern angiographic image acquisition system). Such acquisition systems can also be used to reconstruct 3D images from a sequence of projection from different angles similar to the computed tomography (see Sect. 2.1.5).

Anatomic information from all other structures can be removed when an image is subtracted, which was made prior to giving the contrast agent. Although it is possible—and has been done—to do the subtraction mechanically using film, it is now done on digital images. The technique is called *digital subtraction angiography* (DSA, see Fig. 2.10c).

DSA enhances vessels much more when compared to angiography, but the images may suffer from motion artefacts. This is particularly true in cardiac angiography. Cardiac motion is too fast for creating two images without the heartbeat influencing the result. Gated imaging is possible, but it may be still difficult to choose two images with and without the contrast agent that were taken at exactly the same point in the heart cycle. Furthermore, motion due to breathing and patient movement cannot be removed by gating. DSA images from cerebral blood flow are affected to a much smaller extent by motion artefacts from heartbeat and patient motion.

Motion artefacts cannot be corrected easily because of the location dependency between 3D motion and its projection onto a 2D plane. If corrected at all, motion correction consists of selecting an optimal null image (the image without the contrast agent) from several images, which after subtraction minimizes some error measure. Some research work on nonrigid registration between the two images in DSA has been reported, but as far as we know none of this has reached maturity up to a point that the technique is routinely applied (see Meijering et al. 1999 for a review).

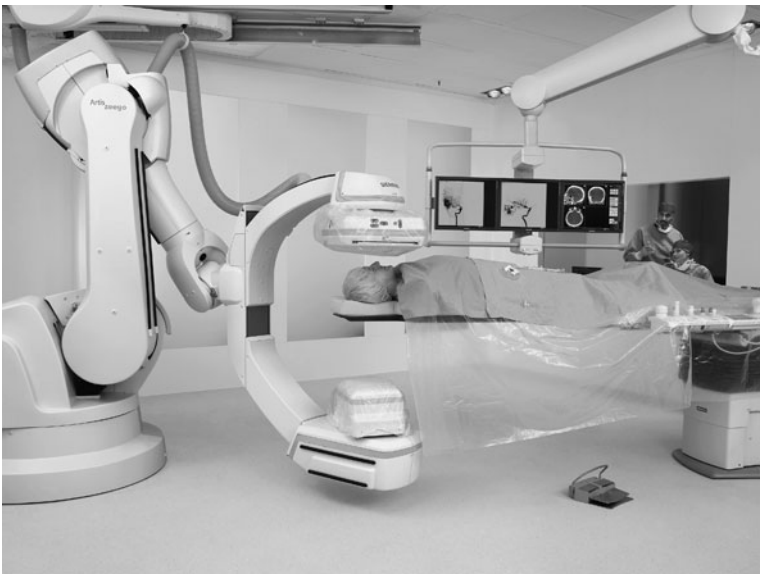

Fig. 2.11 Angiographic imaging device (C-arm) which is used for guiding minimal invasive interventions (Siemens Artis zeego, with kind permission from Siemens Sector Healthcare, Erlangen, Germany)

2.1.4 Mammography

Bremsstrahlung is the major influence in most x-ray tubes with the exception of x-ray tubes for *mammography* (see Fig. 2.12). The purpose of mammography is to detect small, nonpalpable lesions in the female breast. This requires a much higher image quality than normal x-ray imaging with respect to contrast and spatial resolution. Since contrast and resolution are affected by scattering, mammography tubes reduce bremsstrahlung by suitable filtering. Furthermore, mammography tubes use a material (Molybdenum) that produces an almost monochrome x ray with peak energies around 17 to 19 keV. This would be unwanted in regular x-ray imaging as most—if not all—of the radiation would be absorbed and not reach the receptor. For the breast, however, the use of low-energy beams increases the contrast between the subtle differences of different tissues. Using an (almost) monochromatic beam will also reduce scatter, which again increases contrast.

Differences and findings in mammograms are subtle. Hence, *digital mammography* with its potential for postprocessing has received much attention for quite some time (see, e.g., Chan et al. 1987; Dengler et al. 1993; Cheng et al. 1998). Digital mammograms have numerous advantages. They can be easily distributed and accessed in a hospital network. The dynamic range of digital detectors (about 1000:1) is much higher than that of film (40:1). Digital mammograms can be created using currently available TFT flat panel detectors, but owing to the need for a high resolution, the development of techniques reaching an even better resolution is still an active research field.

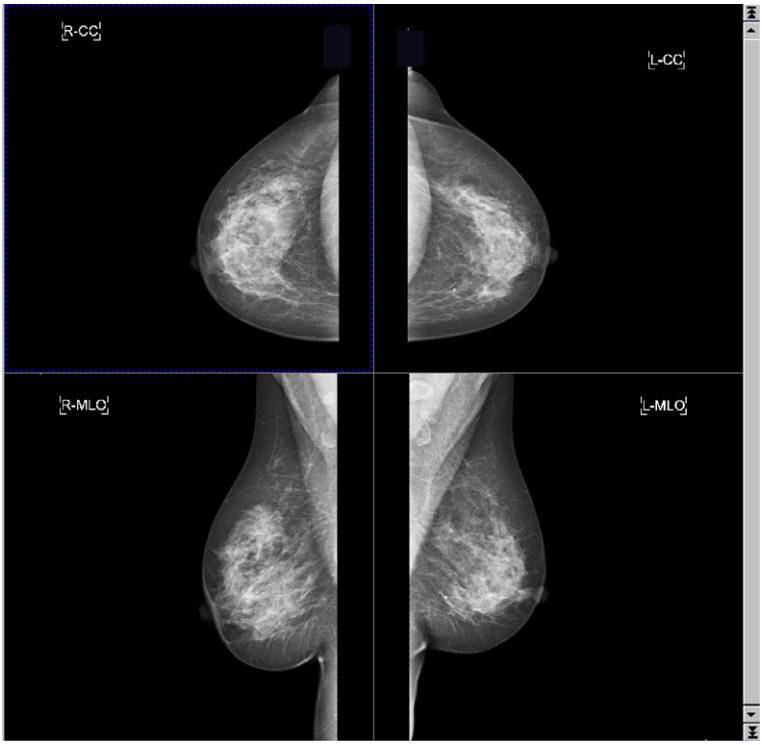

Fig. 2.12 The goal of human or computer-assisted analysis in mammography is to find calcifications which are potential tumor sites (images with kind permission from Siemens Sector Healthcare, Erlangen, Germany)

2.1.5 Image Reconstruction for Computed Tomography

The images from x-ray attenuation discussed so far are projection images. The structures are projected on top of each other. High attenuating objects such as bone may hide other objects. In cranial images, for instance, the skull would hide most of the details of the enclosed soft tissue. Furthermore, the cone beam geometry makes the measurement of absolute distances impossible.[5]

Tomography (from the Greek "tomos" = cut, slice) attempts to create an image of one or more slices through the body. A set of slices provides a detailed 3D distribution of x-ray attenuation per volume unit. The name *computed tomography* (CT, also called CAT = computed axial tomography) emphasizes that these images are not acquired directly by some clever imaging device, but are computed from pro-

[5]There are exceptions, if, e.g., images are made by two different cone beams of a rotating C-arm where the magnification of objects in the center of both cones can be computed.

jection measurements. X-ray computed tomography was invented in the 1970s by Godfrey N. Hounsfield based on the work of Alan M. Cormack[6] (Buzug 2008).

Tomography had been known before as an analogue technique. It produced slices through the body directly on film by moving the film and x-ray source in opposite directions during exposure (Geluk 1979). Depending on the ratio between the speeds of the film cassette and x-ray source, a specific single slice parallel to the image plane was imaged in focus overlaid by blurred layers above and below this slice.

Computed tomography goes a different way. It produces a digitized solution of the inverse *Radon transform* from projections in a slice without interference from other slices (see Buzug 2008 for a detailed treatment of reconstruction techniques). The inversion is computed numerically from projections by the imaging computer.[7]

For a 2D attenuation function $\mu(x, y)$ describing the x-ray attenuation per unit volume in some slice z in the human body, the Radon transform is given by all line integrals through this function

$$R(s,\theta)\left[\mu(x,y)\right] = \int_{-\infty}^{\infty}\int_{-\infty}^{\infty} \mu(x,y)\,\delta(s - x\cos\theta - y\sin\theta)\,dx\,dy, \tag{2.4}$$

where δ is the Dirac-delta function.

In other words, for a given angle θ, the Radon transform produces the projections onto a line s along rays perpendicular to s with angle θ to the x-axis. The Radon transform is invertible, which means that $\mu(x, y)$ may be reconstructed from all projections onto lines s for all angles $0° < \theta < 180°$. This essentially solves the reconstruction problem. Since

$$I_{\text{out}} = I_{\text{in}} \cdot \exp\left(-\int_{t_0}^{t_1} \mu(t)\,dt\right), \tag{2.5}$$

we have

$$\int_{t_0}^{t_1} \mu(t)\,dt = -\ln\left(\frac{I_{\text{out}}}{I_{\text{in}}}\right) \quad \text{with } t = s - x\cos\theta - y\sin\theta. \tag{2.6}$$

If we assume that no attenuation takes place outside of $[t_1, t_2]$, we can extend the bounds of the integral to infinity and

$$R(s,\theta)\left[\mu(x,y)\right] = \int_{-\infty}^{\infty} \mu(t)\,dt = \int_{-\infty}^{\infty}\int_{-\infty}^{\infty} \mu(x,y)\,\delta(s - x\cos\theta - y\sin\theta) \tag{2.7}$$

[6] Alan M. Cormack has been a physicist at the University of Cape Town in South Africa when he developed the theoretical basis for Computer Tomography in the late 1950s. This work was taken up later by Godfrey N. Hounsfield, an electrical engineer at EMI research lab, who presented the first whole body CT scanner in 1975. For their invention, both received the Nobel price of Medicine and Physiology in 1979.

[7] An optical solution for the reconstruction exists as well which has been proposed in the 70s in order to overcome limitations because of lack of computing power (Geluk 1979).

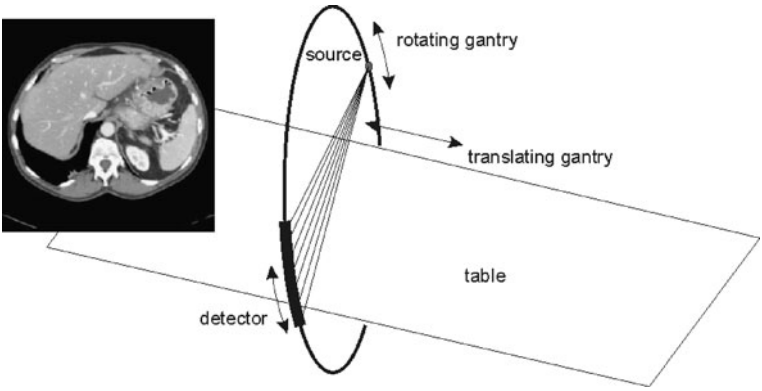

Fig. 2.13 Schematic view of CT image generation. The patient is placed on a moveable table. A CT image is a slice that is reconstructed from multiple projections taken from different angles. A sequence of CTs is created from translating the table and repeating the image acquisition procedure

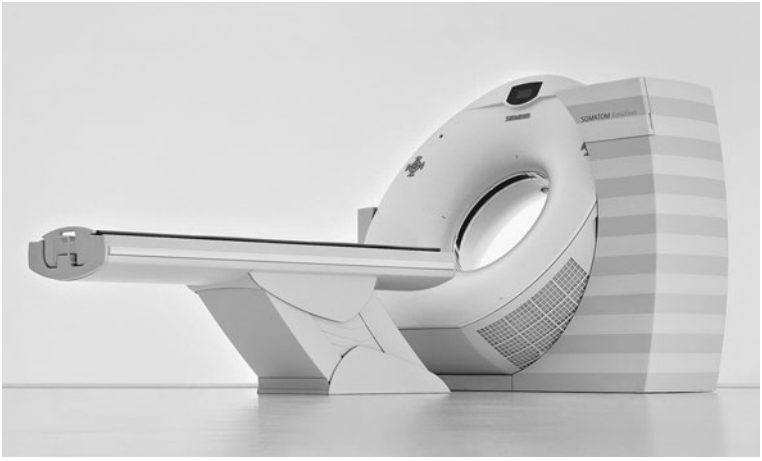

Fig. 2.14 An X-ray CT scanner (Siemens Somatom, image with kind permission by Siemens Sector Healthcare, Erlangen, Germany). Image acquisition takes place in the doughnut-shaped gantry that houses x-ray source and detector rings (which, in this system, can be tilted). The patient is moved through the gantry while slices of CT images are acquired

may be computed from radiographic projections at angles $0° < \theta < 180°$. If we had enough of these projections, the Radon transform could be inverted numerically and a 3D distribution of *attenuation coefficients* is reconstructed.

A CT scanner that acquires projections consists of a single slice or a multiple slice detector ring around which an x-ray source rotates (see Fig. 2.13 for a schematic view and Fig. 2.14 for an image acquisition system). During rotation, detections are constantly made. It can be thought of as a device that creates single

or multiple lines of x-ray images from different angles. Measurements are created much faster than creating complete x-ray images from multiple angles.

Reconstruction by the inversion of the Radon transform creates single or multiple slices of voxels containing attenuation per unit volume in the imaged patient.

A stack of slices is produced by scanning a sequence of different slices or groups of slices. For the scanning process, the patient lies on a table that moves into the detector ring in prespecified steps. The movement is called (translational) *gantry*. The step size of the horizontal movement determines the distance between slices. The thickness of the detector ring determines the slice thickness. Slice thickness is often lower than the distance between slices causing a gap between slices.

The number of slices and their thickness for a CT study has changed dramatically with the advent of multislice scanners. In the early times of computed tomography, a slice thickness of 5 mm with a 5 mm gap or even thicker slices was quite common. A brain image data set from CT may have contained less than 20 slices. A detailed analysis (e.g., of the fine structures in the brain) was difficult to impossible. Newer scanners produced thinner slices, but motion during image acquisition often caused artefacts and image quality deteriorated. An advancement was the development of the *spiral scanner*. In a spiral scanner, the x-ray source rotates in a continuous spiral while measuring absorption data. Resolution and the number of images have been further improved with the use of multislice detectors that acquire more than one slice simultaneously (Buzug 2008).

A body CT study may easily contain 500 to 1000 slices with slice distances of 1 mm or less. Slice thickness may vary, however, because of dose considerations. Thin slices with high resolution may be acquired in the region of interest for capturing as much detail as possible. Slice thickness may be much larger in the context region for providing the necessary anatomic context.

Inverting the Radon transform for slice reconstruction from projections implies parallel projection, whereas x-ray images are acquired in a cone beam projection. It turns out that this is solvable by transformations not essentially affecting the reconstruction method. We thus will assume parallel projection for the remainder of this discussion.

Another problem of image reconstruction is more difficult. The Radon transform assumes a continuous space for s, θ, x, and y. An image will be reconstructed from a limited number of projections and a limited number of measurements per projection. Fortunately, just a finite number of voxels needs to be reconstructed with the attenuation coefficients assumed to be constant within the voxel. Nevertheless, the influence of the digitization on the inversion of the Radon transform needs to be investigated.

Inversion is by means of the Fourier transform, which leads to the *filtered backprojection* (FBP) algorithm. The Fourier transform of the Radon transform delivers what is known as the *Central Slice Theorem*. The theorem states that the Fourier transform $M(u, v)$ of a projection of a function $\mu(x, y)$ in a direction with angle θ to the x-axis equals the coefficients on a line with this angle θ in the frequency space of the Fourier transform of μ (see Fig. 2.15). This can easily be shown for a line with $\theta = 0$, where

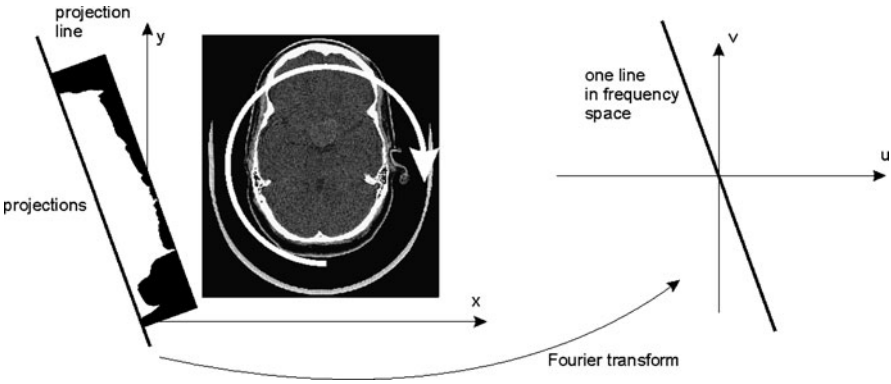

Fig. 2.15 The central slice theorem states that the Fourier transform of a projection onto a line with some angle a equals a line in frequency space of the Fourier transform with equal angle of the image

$$
\begin{aligned}
FFT\big[R(s,0)\big(\mu(x,y)\big)\big] &= FFT\left[\int_{-\infty}^{\infty}\mu(x,0)\,dx\right] \\
&= \int_{-\infty}^{\infty}\left[\int_{-\infty}^{\infty}\mu(x,0)\,dx\right]\exp(-i\,vy)\,dy \\
&= \int_{-\infty}^{\infty}\int_{-\infty}^{\infty}\mu(x,0)x\exp\big(-i\,(0u+vy)\big)\,dx\,dy \\
&= M(x,0). \qquad (2.8)
\end{aligned}
$$

The theorem is true for all other angles θ as well because of the rotation property of the Fourier transform. Hence, projections of $R(s,\theta)[\mu(x,y)]$ for all angles θ are transformed into one-dimensional (1D) frequency space. The coefficients for a projection $R(s,\theta)$ are mapped out on the corresponding line with angle θ in the 2D frequency space. The inverse Fourier transform is then applied for computing the reconstructed image.

There are two problems with this. First, the Fourier transform from projections is defined in a polar coordinate system, whereas coefficients for carrying out the inverse transform are required in Cartesian coordinates. We need to account for the difference in the size of a unit area in polar and Cartesian coordinates. Otherwise, low frequency components in the image would be overly emphasized (see Fig. 2.16). The correction is done by multiplying the Fourier coefficients with $1/r$, where r is the radial distance of a given location (u, v) to the origin. Hence, it is an application of a radial *ramp filter* (see Fig. 2.17 for a filtered reconstruction).

Second, the distribution of Fourier coefficients from polar coordinates becomes sparser in the high frequency range of the Cartesian coordinate system. It may cause artefacts because noise often predominates in the high frequency range. Hence, projections are usually low-pass filtered, by filters such as the *Hamming window* or *Hamming filter* (see Sect. 4.3 on image enhancement).

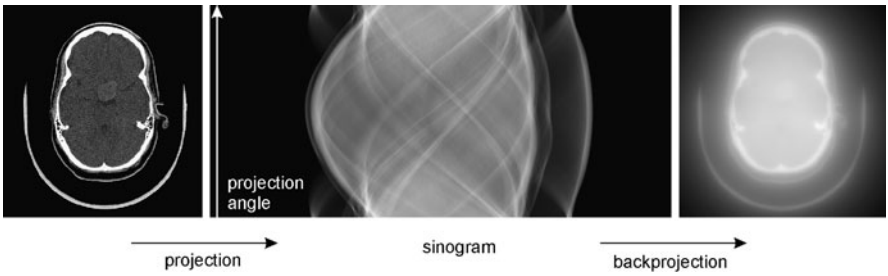

Fig. 2.16 Projecting along angles between 0° and 180° produces a projection image (which is also called sinogram). Unfiltered reconstruction results in artefacts because the varying density of Fourier coefficients has not been accounted for

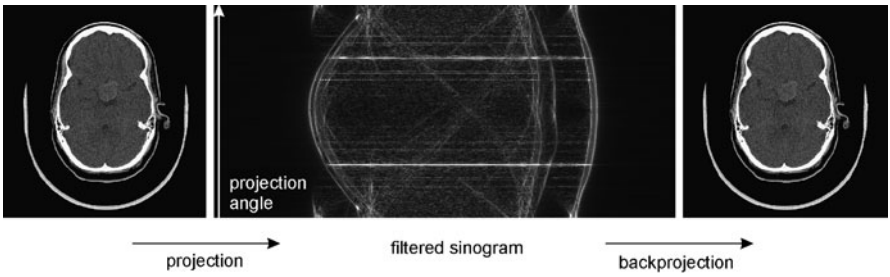

Fig. 2.17 Filtering the projection with a ramp filter that attenuates amplitudes with decreasing frequency removes artefacts from simple reconstruction

The inversion of the Radon transform using the Central Slice Theorem does not really require transforming the projection data into frequency space. The Fourier transform is a linear operator. Adding terms for the Fourier transform or its inverse may be carried out in any order. One particular order would be to transform a line s of the projection data, filter the result and invert the transformation, and then carry on with the next line. If we look at the process more closely, we see that this can be replaced by convolving the projection data of this line with a convolution function that is the spatial domain equivalent of the filter function, and then project the result perpendicular to s onto the image. This is to be done for every projection and gives the method its name *filtered backprojection* or *convolution backprojection reconstruction*.

The reconstruction result is a digital image of attenuation coefficients for each voxel with the thickness of the slice and a size along x and y according to the chosen in-plane spatial resolution. Common image sizes for CT images are 512×512 or 256×256. The size of the voxel along the x- and y-axes depends on the field of view (FOV), which depends on the opening angle of the cone beam scanning the patient. For brain images with an FOV of about 30×30 cm^2, in-plane voxel sizes for a 512×512 image are 0.5×0.5 mm^2.

Table 2.1 Hounsfield units of different tissues. Air, water and bone are well-differentiated, while contrast between different soft tissues is low

Air	Fat	Water	Blood	Muscle	White matter	Grey matter	CSF	Bone
−1000	−100	0	30–45	40	20–30	37–45	15	>150

Attenuation coefficients are normalized for making the result independent of imaging parameters such as beam energy. The scale is called the *Hounsfield scale.* Normalization is based on the attenuation μ_{Water} of water and μ_{Air} of air

$$HU(\mu) = 1000 \cdot \frac{\mu - \mu_{\text{Water}}}{\mu_{\text{Water}} - \mu_{\text{Air}}}. \tag{2.9}$$

Thus, air has −1000 HU (Hounsfield units) and water has 0 HU. Hounsfield units for different tissue types are given in Table 2.1. Hounsfield units are mapped to integers and usually represented in a range from −1000 to 3000. Hence, attenuation coefficients can be represented by two byte integers.

The display software of a scanner system lets the user choose an appropriate HU range to be mapped onto the displayable range of 256 gray values by specifying the *window* (the width of the range to be mapped) and the *level* (the value to be mapped onto the gray value 128). Different window and level settings are used to emphasize different tissues. A bone window, for instance, will have a high level and a large window because attenuation for bone is high and extends over a wide range. A lung window, on the other hand, will have a much lower level since most of the lung is filled with air.

Air, fat, water, and bone have significantly different attenuation, whereas the differences between the various soft tissues are small (see Table 2.1). In fact, the results from the first experiments of CTs of the head were not overwhelming and medical equipment companies were reluctant to build a CT scanner.[8] Scanners have much improved since then in terms of spatial resolution as well as in terms of suppressing noise and artefacts. CT is probably still the most often used digital image device in diagnosis and surgical intervention. Typical application areas for diagnostic imaging are bone CT, CT of the brain, and CT of the parenchyma.

A number of artefacts may occur when creating the image by FBP, which have to be accounted for in a later image analysis.

- *Noise* (Fig. 2.18) is caused from scatter in the patient and at the detector. Since the likelihood of a photon reaching the detector unscattered can be modeled as a Poisson process, the noise is often modeled by a Gaussian function (which is a good approximation of a Poisson distribution for large numbers of events).
- The *partial volume effect* (PVE, Fig. 2.18) occurs because attenuation within a voxel may not be uniform. The PVE within a slice is usually easy to recognize. It is most prominent between adjacent voxels with very different attenuation coefficients such as at the bone-CSF boundary. The reconstructed attenuation coefficient will be a value between that of the two tissues. The PVE occurs between

[8] The first CT scanner was built by a record company (EMI).

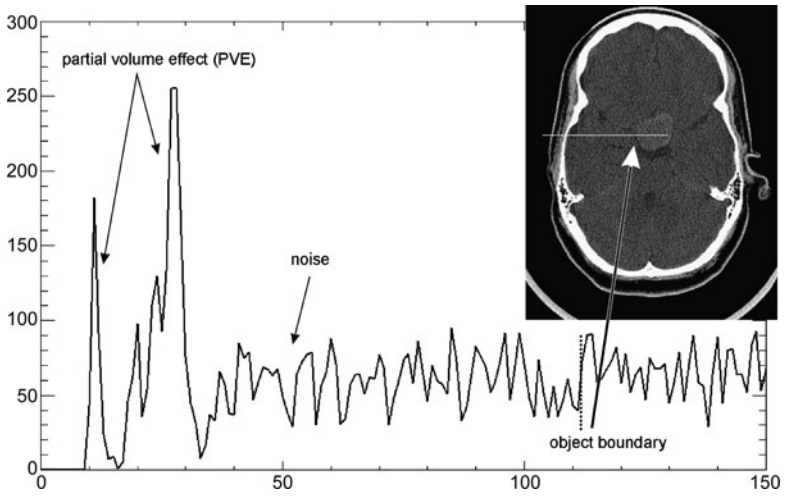

Fig. 2.18 Noise and the partial volume effect (PVE) in CT imaging. The PVE causes blur at skin, fat, bone and CSF boundaries. Noise amplitude in this image is in the range of the signal increase at the object boundary

slices as well and may be less obvious because the object causing the PVE may be in the slice above or below the currently displayed slice.

- *Metal artefacts* are caused by the very high difference between the attenuation of metal and tissue. This makes the reconstruction less robust against other influences such as noise and PVE.[9] It results in severe *streak artefacts*. Such artefacts can be observed at all high contrast boundaries, but are particularly severe in the case of metal artefacts.
- *Motion artefacts* are the result of voluntary or involuntary patient movement (movement due to breathing, heartbeat, etc.) during the acquisition of a single slice. Motion violates the assumption that attenuation at some location (x, y) is the same for every projection and causes blur in the image. Since the influence from motion may be different for different slices, it may cause the so-called *step-ladder-artefact* between slices (visible in reoriented views, see, e.g., Ghersin et al. 2006).

Tomographic imaging using x rays can also be carried out using x-ray equipment for projection images. Early attempts included the use of image intensifiers for rapid imaging of the heart (Mayo Clinic; Robb et al. 1982). Newer developments employed angiographic acquisition systems for reconstruction (Ning et al. 2000; Akpek et al. 2005). Since angiography uses a moveable and rotatable C-arm, projections can be reconstructed from programmed C-arm rotation. The receptor device is a TFT flat panel detector with up to 1000×1000 elements. Each projection si-

[9]The problem of image reconstruction can be stated as an algebraic problem of finding unknowns—the attenuation—from linear equations—the projections—and it can be shown that the problem becomes more ill-conditioned when some very high attenuation regions exist.

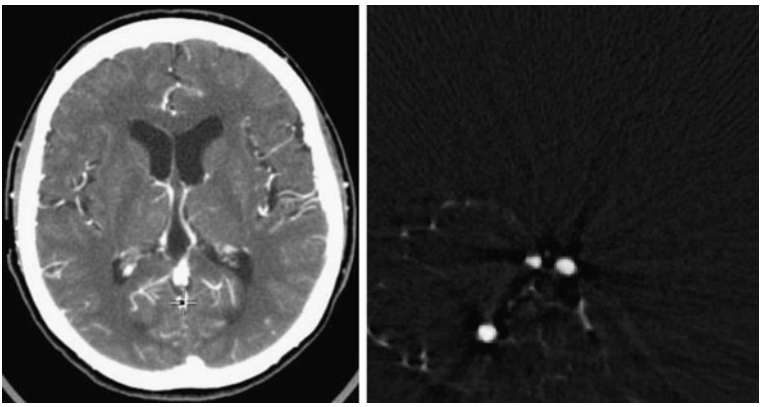

(a) (b)

Fig. 2.19 CT angiography (**a**) shows contrast-enhanced vessels. While showing also tissue in the context, vessels are more difficult to detect than in reconstructed DSA images (**b**)

multaneously acquires data from 1000 slices with 1000 projections per line. Reconstructed images thus have a higher spatial resolution than ordinary CT images and produce all slices at the same time. It comes at a cost, however. Current systems are not fast enough to generate projections from as many angles as a conventional CT system. In consequence, artefacts due to an insufficient number of measurements increase. The images are noisier and the streak artefacts are more pronounced.

2.1.6 Contrast Enhancement in X-Ray Computed Tomography

The contrast agent used in fluoroscopic imaging or angiography is used in x-ray CT as well. Instead of showing a time-varying function such as in fluoroscopy, the use of a contrast agent in x-ray CT enhances structures that are otherwise difficult to differentiate. A major application is the depiction of vessels (*CT angiography* or CTA; Dillon et al. 1993).

CTA works similarly to ordinary x-ray angiography with the difference being that the images are not projections (see Fig. 2.19a for an example). The 3D nature of CTA images allows quantitative analysis by direct measurement on the image. With the spatial resolution of today's scanners, diagnosis of the extent of a stenosis becomes possible through CTA even for smaller vessels. It needs to be kept in mind, however, that CTA requires a higher exposure to x rays than x-ray angiography. Compared to subtraction angiography (a reconstruction from DSA is depicted in Fig. 2.19b), CTA provides information about soft tissues not visible in DSA. On the other hand, the intensity of vessels filled with the contrast agent is similar to that of bone, making it difficult to separate the vessel structures close to the skull from bone structures.

2.1.7 Image Analysis on X-Ray Generated Images

Radiographs have a high spatial resolution which supports the detection of small lesions such as microcalcifications in mammography, potentially cancerous nodules in lung scans, or small stenoses in angiography. The signal is bright for dense structures and dark for low attenuation objects.

As the image is a projection, no assignments between absolute brightness value and tissue type can be made. Distance measurements are not possible, except for measurements of distance ratios between structures of which the approximate distance to the radiation source is known to the radiologist. Overexposure or underexposure (for digitized film) may reduce the contrast and the images may be blurred due to motion or the size of the focal spot.

Recognition of small objects may be hindered by the fact that structures hide other structures in the projection. Projection may also cause a very convoluted appearance of larger objects (such as complex bone fractures), which bears little resemblance to the actual shape of this object. Deducing the true geometry of such an object from its projection may be easy to the experienced radiologist, but difficult to implement in an algorithm. It requires extensive context knowledge about the projection direction, the orientation of the organs being imaged, and their relative position with respect to the projection direction.

Creating tomographic images reduces or removes some of the problems above, which is one of the reasons for the sudden increase of computer-assisted analysis methods in medicine with the appearance of CT imaging in the 1970s. CT images have a lower spatial resolution than radiographs, which is why radiographs may still be preferred if the diagnosis requires high resolution images.

If noise, partial volume effects, and other artefacts are disregarded, a mapping between the tissue type and attenuation coefficient exists in a voxel of a CT. The normalized attenuation coefficients of the Hounsfield scale make mappings from different images created by different machines comparable. The value of this is not to be underestimated. Even though the mapping is only approximate and distorted by artefacts and even though it is certainly not invertible (i.e., a certain HU value is not uniquely associated with a certain type of tissue), it comes close to the primary goal of imaging (i.e., directly measuring and displaying the tissue and tissue characteristics).

2.2 Magnetic Resonance Imaging

Protons and neutrons of the nucleus of an atom possess an angular momentum that is called *spin*. These spins cancel if the number of subatomic particles in a nucleus is even. Nuclei with an odd number exhibit a resultant spin that can be observed outside of the atom. This is the basis of *magnetic resonance imaging* (MRI) (Liang and Lauterbur 2000). In MRI, spins of nuclei are aligned in an external magnetic field. A high frequency electromagnetic field then causes *spin precession* that depends on the density of magnetized material and on its molecular binding. The resonance of

the signal continues for some time after this radio signal is switched off. The effect is measured and exploited to create an image of the distribution of the material.

The resonance effect has been used in MR spectroscopy for quite some time. A detailed description of MR spectroscopy and its clinical applications can be found in Salibi and Brown (1998). However, imaging (i.e., the computation of the spatial distribution of effects from magnetic resonance) did not exist before the 1970s. Image generation with magnetic resonance is due to Paul C. Lauterbur and Peter Mansfield.[10]

Magnetic resonance imaging almost exclusively uses the response of the hydrogen nucleus which is abundant in the human body. Variation of hydrogen density and specifically its molecular binding in different tissues produces a much better soft tissue contrast than CT. MRI has some further advantages if compared with x-ray CT.

- MRI does not use ionizing radiation.
- Images can be generated with arbitrary slice orientation including coronal and sagittal views.
- Several different functional attributes can be imaged with MRI.

In summary, MRI is a remarkably versatile imaging technique justifying an extended look at the technique.

2.2.1 Magnetic Resonance

As mentioned above, nuclei with an odd number of protons or neutrons possess a spin. To produce a resonance image, spins of all nuclei of the body are aligned in a static magnetic field B_0. The strength of the magnetic field is measured in Tesla (T) or gauss (10,000 Gauss = 1 T). Today's MR imaging devices for human full body imaging operate with field strengths between 1 and 3 T.

The static field causes spins to be aligned either parallel or antiparallel to the magnetic field. The strength of the measurable signal depends on the difference between these two types of alignment. This, in turn, depends on the type of atom, on the magnetic field strength and on the temperature at which the measurement takes place. The atom-specific sensitivity is highest for hydrogen.

A precession of spins around an axis parallel to the B_0-field can be induced by a radio signal. The effects of parallel and antiparallel precessing spins cancel. For hydrogen at normal room temperature and a magnetic field of 1.5 T, the ratio between the parallel and antiparallel spins is approximately 500.000:500.001. Hence, the observed net signal from all spins will come from just one in a million protons (see Fig. 2.20).

[10]Peter Mansfield is a British physicist who provided the basis for interpreting the signal from resonance. Paul C. Lauterbur is a chemist who first provided the methodology for turning the signal into an image. For their achievement, both received the Nobel price for Physiology and Medicine in 2003.

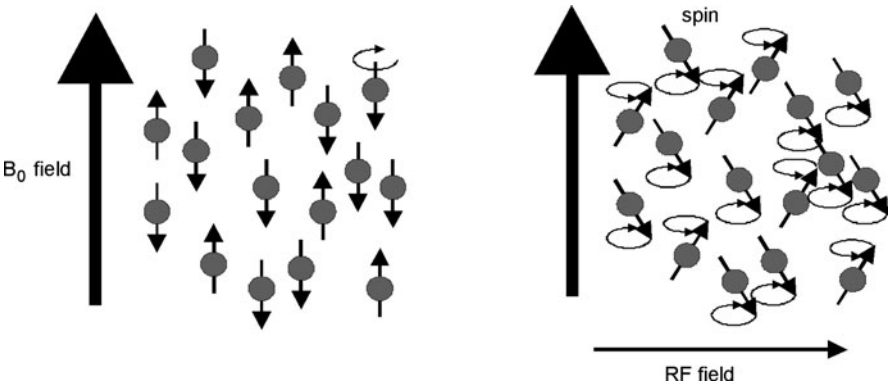

Fig. 2.20 Spins are aligned parallel or anti-parallel to the B_0-field. They produce a signal induced by an RF field. Just a small excess amount of protons aligned parallel produce the signal, since signals from parallel and anti-parallel aligned protons cancel

Given that the hydrogen atom possesses the highest sensitivity of all atoms and that the temperature cannot be increased arbitrarily, the only way to increase the signal is to increase the magnetic field. This is the reason for the exceptionally high magnetic fields that are applied in MRI (for comparison, the strength of the Earth's magnetic field is 0.00003–0.00006 T).

If spins are aligned in the external B_0-field, their angular momentum (i.e., their spin frequency ω) depends on the strength of B_0 and an atom-specific *gyromagnetic constant* γ

$$\omega = \gamma B_0. \tag{2.10}$$

The frequency ω is called the *Larmor frequency*. The gyromagnetic constant for water is 42.58 MHz/T, which translates into a spin frequency of 63.87 MHz for an MRI scanner with a static field with 1.5 T.

To produce resonance, additional energy is supplied causing the spins to precess around the direction of the B_0-field.[11] It is applied by an electromagnetic field that is perpendicular to B_0. The field effects proton spins only if it changes with the same frequency than the rotation frequency of the spins. Hence, if the strength of the B_0-field would be 1.5 T, the required frequency of the resonance triggering field would be 63.87 MHz. This high frequency field (HF) radio wave is supplied by a radio antenna.

The radio signal tilts the spins by an angle $0° < \alpha < 180°$ from their rest direction. The magnitude of the angle depends on the energy of the HF field signal (see Fig. 2.21). After the signal is switched off, the spins slowly return into their rest direction parallel or antiparallel to the B_0-field while still carrying out the precession.

[11] The following discussion relates to effects observed in voxels containing a large enough number of photons so that quantum effects can be neglected.

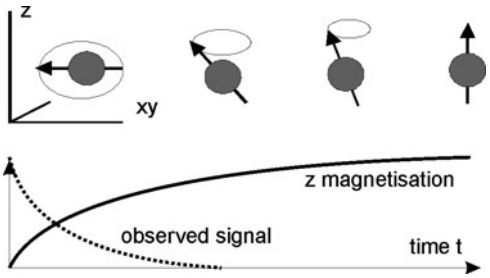

Fig. 2.21 Free induction decay experiment: spins of excited hydrogen atoms are projected into the *xy*-plane orthogonal to the B_0 magnetic field. After switching of the RF signal, the original z-magnetization is restored with time constant T_1. The observed signal decreases much faster since spins start to dephase

This can be measured by an antenna (which could be the sender of the HF field acting as receiver). The observed decreasing signal is called *free induction decay* (*FID*). Its amplitude depends on several factors.

- The amplitude is proportional to the number of spins. Hence, amplitude per unit volume is proportional to the *proton density*.
- Spins returning to their rest direction will deliver a signal of decreasing magnitude, which will cause the FID signal decay with time. The restoration of the original spin direction is called *longitudinal relaxation*. Magnetization $M_z(t)$ in the z-direction (the direction of the B_0-field) at time t is

$$M_z(t) = M_0\big(1 - c \cdot \exp(-t/T_1)\big), \tag{2.11}$$

  with M_0 being the magnetization in M_0 before excitation. The time constant of the exponential relaxation is called T_1*-time*, *spin-lattice-relaxation time*, or *longitudinal relaxation time*.
- Spinning protons act as magnets and influence the behavior of adjacent protons. The precession of spins will dephase with time and the observable FID signal will vanish long before the original magnetization in the z-direction is restored since the antenna measures a vector sum of all spins (see Fig. 2.22). The signal decay is exponential as well, and is described by a constant that is called T_2*-time*, *spin-spin-relaxation time*, or *transverse relaxation time*. If $M_T(t)$ is the transverse magnetization perpendicular to z at time t, then

$$M_T(t) = M_T(0) \cdot \exp(-t/T_2). \tag{2.12}$$

T_1 and T_2 constants for the same proton differ depending on the proton's molecular binding. Protons in water have a larger T_1 than in soft tissue, while T_2 is smaller in soft tissue. T_1 and T_2 in water are in the range of seconds.

Additionally to the tissue-specific attributes, an unwanted effect causes a much faster signal decay than T_2 relaxation. Signal generation is made under the assumption that the static B_0 field is constant everywhere in the imaged region. Even small

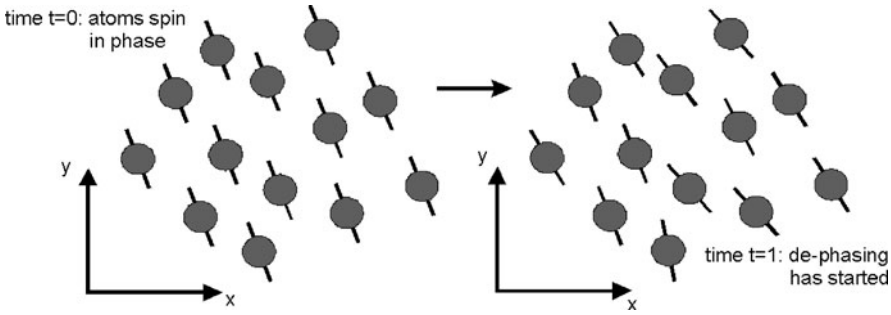

Fig. 2.22 Immediately after the RF signal is switched off, all spins are in phase giving the maximum signal. Locally different magnetization from neighboring atoms causes dephasing as does inhomogeneity of the B_0 field. The observed net magnetization decreases, since its magnitude is the magnitude of the vector sum of all protons in a voxel

field variations cause a much quicker dephasing of spins than dephasing by spin–spin relaxation. Signal decay due to an inhomogeneous magnetic field is exponential with a constant T_2^*. The T_2^* effect is unwanted, as it interrogates the homogeneity of the magnetic field, but not the chemical composition of the probe to be imaged.

The resonance signal allows analyzing the chemical composition of a probe in MR spectroscopy. Instead of exciting just hydrogen, the occurrence and density of other atoms with an odd number of protons or neutrons may be measured by applying a frequency band encompassing all the frequencies necessary to excite the respective atoms. Frequency analysis and the measurement of decay times enables the separation of the signal in constituents caused by the different materials. For imaging, however, additional measures need to be taken to localize the MR signal.

2.2.2 MR Imaging

Extending the MR technique for creating an image is due to the work of Mansfield and Lauterbur. The dependency of the excitability of a proton on the frequency of the HF field is used for the necessary localization. It requires additional *gradient magnetic fields* (called x-, y-, or z-gradient according to the direction of increasing field strength).

If, before applying the HF field, a linear gradient field in the z-direction is overlaid to the B_0-field, the magnetic field strength will linearly increase in the direction of z. Protons will spin with a frequency that depends on their location in z. If an HF field is applied whose frequency range corresponds to the spin frequencies of protons in a slice with $z_1 < z < z_2$, only those protons will be excited and produce a resonance signal (see Fig. 2.23). The process is called *slice selection*. After excitation, the z-gradient is switched off and protons in the selected slice spin with a frequency as determined by the B_0-field.

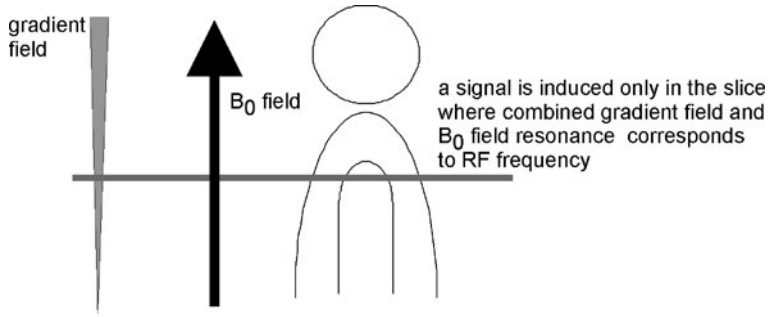

Fig. 2.23 Slice selection is done by selecting an RF band that corresponds to a specific resonance frequency band given by the B_0 field and the slice selection gradient

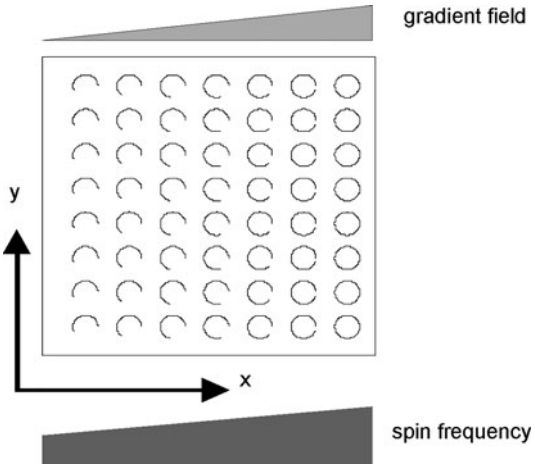

Fig. 2.24 Frequency encoding of the signal is done by a gradient field in the xy-plane. It causes spins to rotate with different frequencies at readout time, so that atoms can be associated to lines orthogonal to the gradient field

To localize protons within a slice, a similar technique is applied while reading the signal. If a linear gradient field in the x-direction is applied during the observation of the resonance signal, the recorded signal will contain a range of frequencies (see Fig. 2.24). The process is called *frequency encoding*. The gradient is called *readout gradient*. Frequencies w_0 to $w_{\max}$ correspond to x-values x_0 to $x_{\max}$. The resonance signal is then transformed into frequency space. The amplitude value at frequency $w_0 + (w_{\max} - w_0) \cdot (x_k - x_0)/(x_{\max} - x_0)$ corresponds to the response of all protons on the line $x = x_k$.

The technique produces a projection of spin densities along y onto the x-axis. A complete set of projections can be obtained by adding projections at measurements with gradient fields along different directions. Having obtained the data, an image could be reconstructed by filtered backprojection. This was the first technique for reconstructing MR images.

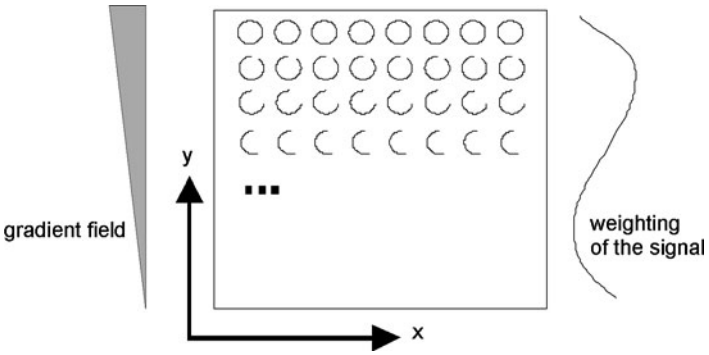

Fig. 2.25 The gradient field for each phase encoding causes a controlled dephasing which acts as a weighting of the observed signal with a cosine function. Phase encoding is done before readout and the phase encoding gradient is switched off before readout

Today's scanners employ a different technique, which is called k-space imaging (k-space is another word for frequency space). k-space imaging generates the image function in frequency space directly through measurements. The first line in k-space is already the result of frequency encoding as described above. It produces the integral of spin densities along the lines of the constant y-value and can be interpreted as the first line of values of a Fourier transform in the u-direction (containing the coefficients with frequency 0) assuming that the Fourier transform maps (x, y) to (u, v).

Let us now consider the signal before applying the frequency encoding gradient. If we apply another linear gradient in the y-direction prior to making the measurement, spin frequency will increase along y and the spins will dephase. The gradient is called the *phase encoding* gradient. It is applied just long enough to dephase spins between 0 and 2π for the range of y-values between y_0 and $y_{\max}$. After switching off phase encoding, frequency encoding is applied and the obtained signal is transformed into frequency space. The results are integrated spin densities along x weighted with a cosine wave of frequency 1 for each line of constant y. In other words, we have produced the real-valued part of the next line in k-space of the Fourier transform in the u-direction (see Fig. 2.25). The imaginary part is computed by weighting the signal with the corresponding sine wave.

The measurement is repeated with phase encoding for the remaining lines in k-space. Once the k-space is filled, the image is generated by transforming it back into the spatial domain.

The image equipment looks similar to CT (see Fig. 2.26). However, the gantry in which the B_0-field is produced is usually smaller than a CT gantry. Image planes need not to be perpendicular to the direction of the B_0-field since the gradients may be generated in arbitrary directions. It is a major difference compared to CT imaging. Also, a variety of different images may be produced of the same patient showing different aspects of the resonance signal. Three different parameters—spin density ρ, spin-lattice relaxation T_1, and spin–spin relaxation T_2—determine the

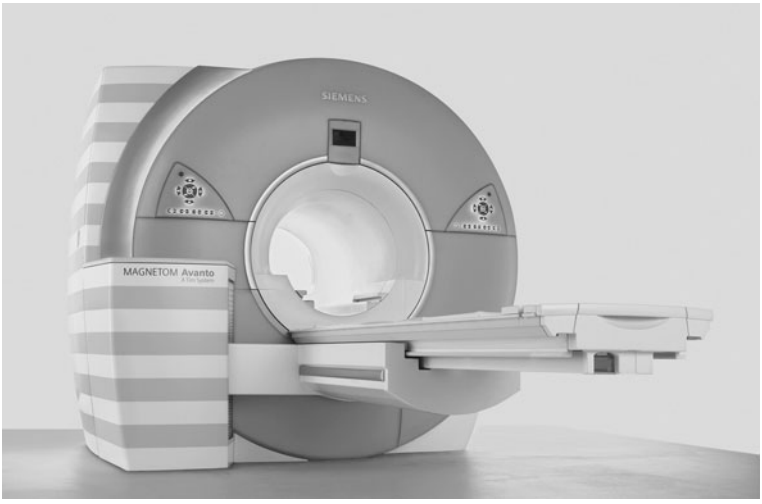

Fig. 2.26 Gantry of an MR imaging device (Magnetom Avanto, with kind permission from Siemens Sector Healthcare, Erlangen, Germany). Images can be produced at arbitrary angles with respect to the gantry by producing appropriate slice selection gradients

resonance signal. Hence, different sequences can be developed for enhancing either of the parameters (some of the major sequences used in MR imaging will be discussed in the next section; a more detailed treatment can be found in Liang and Lauterbur 2000). It changes the appearance of different tissues in images (e.g., water and fat is bright in T_2 images and tissue is darker while the opposite is true for a T_1 image). A normalized scale such as the Hounsfield units of CT does not exist.

2.2.3 Some MR Sequences

T_1 and T_2 time constants cannot be measured directly because signal strength is always influenced by proton density and because field inhomogeneities (the T_2^* decay) hide the T_2 effect. T_2-enhanced images can be generated by the *spin echo* sequence. The sequence uses a clever mechanism to cancel out T_2^* effects. It consists of a 90° impulse that tilts spins into the *xy*-plane followed by a sequence of 180° impulses producing spin echoes.

After application of the 90° impulse spins start to dephase due to the combined influence of spin–spin relaxation and field inhomogeneities. Spin–spin relaxation continues after application of the 180° impulse since relative spin orientation although turned by 180° remains the same. T_2^* influence is inverted, however, because higher frequency spins, which had a positive phase difference, now have a negative phase difference with respect to spins with lower frequency. Spins will rephase with respect to field inhomogeneities and produce the first echo of T_2-relaxation (see Fig. 2.27). They dephase again until the next 180° impulse causes the next echo. The envelope containing the echoes decreases exponentially with T_2.

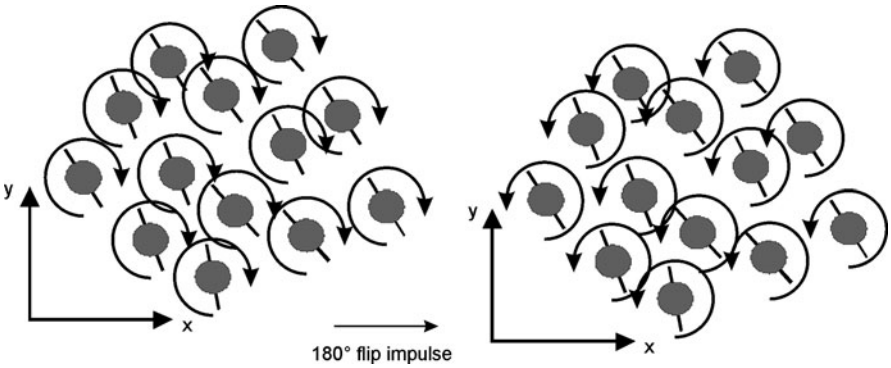

Fig. 2.27 The spin-echo sequence causes dephasing spins to rephase by flipping by a 180° impulse which reverses the direction of precession

Usually, a single echo will be taken as the image. The time between the 90° impulse and the echo impulse is called *echo time TE*. The time between two measurements is called *repetition time TR*. Short *TE* (20 msec) and long *TR* (2000 msec) will produce a proton-density-weighted image. Using a shorter repetition time ($TR = 300$–600 msec) will produce a T_1-weighted image because T_1 relaxation is generally longer than 200–600 msec. A long *TE* (> 60 msec) and a long *TR* (2000 msec) produces a T_2-weighted image.

The *inversion recovery* sequence is another sequence used in MRI. It produces an image that is strongly influenced by the T_1 time constant. In inversion recovery a 180° impulse is followed by a 90° impulse. The time between the two impulses is called *TI* or *inversion time*. The 180° impulse leads to saturation (i.e., a new impulse would not produce a signal). However, after time *TI* protons have recovered their longitudinal magnetization to an extent that depends on their individual T_1 time. Hence, they are able to produce a resonance signal from the 90° impulse. An echo at echo time *TE* rephases spins that are then read out. Long inversion times ($TI > 2000$ msec) and short echo times ($TE = 10$ msec) produce a proton-density-weighted image. Shorter inversion times (400–800 msec) with the same echo time produce a T_1-weighted image, while choosing a long echo time ($TE > 60$ msec) will produce an image that is T_2-weighted.

MR images of the head created by imagining sequences like the ones above usually have a slice thickness of 1 to 3 mm and 256×256 voxels in a slice. Body MR images usually have 512×512 voxels per slice. Data acquisition times using either of the sequences are longer compared to CT imaging. For reconstructing an image of size 256×256 pixels, 256 lines in k-space need to be measured. This requires 256 different measurements. A new measurement is only possible after the effects from the previous measurement have decayed. With T_1-time constants in the range of a second, it results in repetition times in the range of several seconds. It leads to data acquisition times for the image in the range of 10–15 minutes. If the image size doubles, the acquisition time doubles as well. If measurements are repeated to increase the signal-to-noise ratio or if more than one measurement is desired, ac-

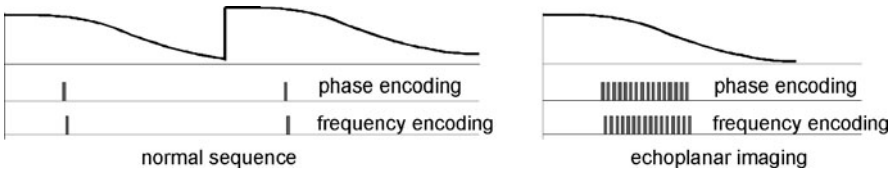

Fig. 2.28 The main difference between normal encoding and a fast imaging sequence is that in fast imaging several to all encodings are done during a single excitation of the resonance signal

quisition times for a full study may easily reach 30–60 minutes. The acquisition of a sequence of slices, however, does not necessarily take much longer. Since slice selection only influences protons of a given slice, signals from several slices may be acquired in an interleaved mode.

In the early 1980s, acquisition times have been a serious drawback. Since the 1990s, a wealth of fast imaging sequences have been developed. *Gradient echo imaging* was one of the first techniques to speed up imaging time. In gradient echo imaging an excitation pulse of α (with $\alpha \leq 90°$) is given. However, instead of using the 180° impulse to produce a rephased spin echo, an inverse gradient is applied to cause the echo. Echo times between applying the second gradient and readout are much faster than echo times of the spin echo sequence. Pulses with α close to 90° produce a T_1-weighted image. Low angle pulses result in a T_2^*-weighted image. The image is not T_2-weighted because, as opposed to spin echo imaging, the gradient echo reverses dephasing from inhomogeneities and spin-spin relaxation in the same way.

Turbo spin echo sequences make several measurements at a time. This is done by applying a sequence of several phase shift gradients during a single echo and reading the signal after each phase shift (see Fig. 2.28). Several lines of k-space are filled at the same time and image acquisition time decreases by a factor of the number of lines acquired per repetition. In its extreme, all lines are acquired from a single excitation (RARE—Rapid Enhancement with Relaxation Enhancement) so that an image can be acquired within time *TE*. RARE is a variant of an older sequence known as Echoplanar Imaging (EPI), a term which simply refers to acquiring the complete k-space in a single resonance experiment.

2.2.4 Artefacts in MR Imaging

Ultrafast sequences such as EPI produce images in less than 100 msec. There are problems, however. While making the measurements from a single echo, T_2^* dephasing continues to occur. Different lines in k-space are measured with a different contrast with respect to T_2^* decay. Moreover, the number of lines to be measured in k-space is usually restricted to 128 or less so that the spatial resolution of a single shot image does not exceed 128 × 128 pixels. Furthermore, artefacts from chemical shift, ghosting, and shading may be particularly pronounced for fast imaging sequences.

The *chemical shift* of protons (and any other nuclei) is caused by magnetic shielding from electrons in the molecular environment. It depends on the molecular binding of protons and causes a material-dependent deviation of spin frequency. The difference is particularly apparent for protons in water, as compared to those in fat. Since frequency encoding interprets the measured frequency as location, water protons will be reconstructed at an offset to fat protons in the frequency encoding direction. Chemical shift is present in all nonshift-corrected images, but is pronounced in EPI (RARE) images where the offset may amount to 8–10 pixels. At 3-mm voxel size this is an offset of about 2.5 cm.

Ghosting appears because of the inaccuracies in the phase encoding. If one or more lines in k-space are phase shifted, the corresponding waves in the spatial domain are shifted as well. Ghost images appear in this direction. Ghosting may also happen in regular imaging if the patient has moved in the phase encoding direction between acquisitions. Motion in the direction of frequency encoding causes the much less prominent blurring artefact similar to this kind of artefact in CT.

Shading is due to the variation of attenuation of the RF signal and an inhomogeneous magnetic field. It causes differences in the resonance signal according to location. It is then turned into different intensities to be reconstructed for the same material at different locations.

Artefacts from noise and PVE are similar to CT imaging. Metal artefacts from paramagnetic materials cause signal deletion. The presence of ferromagnetic materials such as implants is a contraindication for MR imaging as is the presence of implanted electronic devices such as a pacemaker.

2.2.5 MR Angiography

MR angiography (MRA) exists with and without using contrast agents. Contrast-enhanced angiography uses *gadolinium*, an agent that causes a strong decrease of the T_1 relaxation time. Gadolinium-enhanced vessels can be imaged with a T_1-weighted sequence that saturates all other tissues while highlighting the vessels. The resulting contrast is so high that the images look similar to DSA images, but without the necessity of subtracting a null image (see Fig. 2.29a). Vessels may be depicted even if they are smaller than a voxel because of the partial volume effect.

MRA images come as a true 3D volume, but they are often displayed as *maximum intensity projection* images (MIP). This visualization technique projects the brightest voxel along the projection line on a pixel on the output screen. MIP is simple, fast, and produces images similar to digital subtraction angiograms.

MR angiography without the use of a contrast agent exploits two different effects, which are called *flow void* and *phase contrast angiography* (Dumoulin 1995). A flow void occurs when a proton that has been excited by an HF impulse has moved out of the slice before the readout impulse is applied.

Phase contrast angiography uses the motion artefact of moving blood for imaging. If a proton moves in the direction of the phase encoding gradient, it carries its phase with it (see Fig. 2.30). Two different phase encoding gradients are applied at

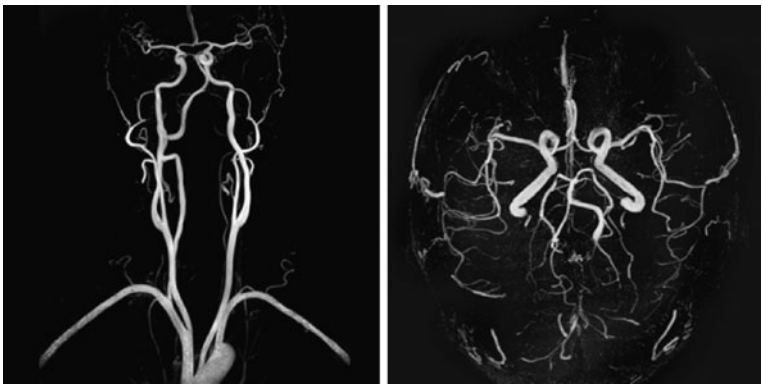

Fig. 2.29 Maximum intensity projections of gadolinium-enhanced MRA (*left*) and phase-contrast MRA (*right*). While using gadolinium contrast agent produces images with better resolution, phase contrast imaging is non-invasive and has the potential for computing vessel velocities (images from Siemens Sector Healthcare with permission)

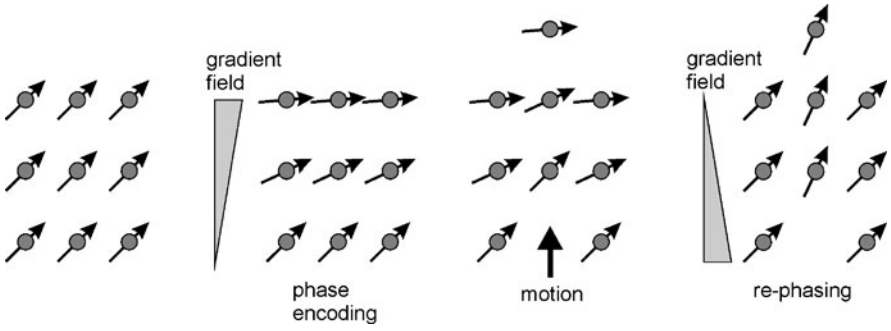

Fig. 2.30 Principle of phase-contrast imaging: protons are phase-encoded by applying a gradient field. Motion in phase encoding direction leads to dephasing. If a rephasing gradient is applied, dislocated protons cause a signal loss since they are not completely rephased. The amount of signal loss depends on the motion in phase encoding direction

times t_1 and t_2. The second gradient is exactly opposite to the first gradient. The effects of the gradients on protons that have not moved between t_1 and t_2 will cancel. Protons that moved along the gradient direction will acquire a phase shift relative to static protons, which is proportional to the distance traveled between t_1 and t_2 (i.e., proportional to their speed). A 3D velocity vector for moving protons can be created by applying phase encoding in the x-, y-, and z-directions. Velocity indicates the existence of a vessel (see Fig. 2.29b). Suggestions have been made that phase contrast angiography may even enable the analysis of velocity differences in blood vessels (e.g., at a stenosis or in an aneurysm).

2.2.6 BOLD Imaging

Blood supplying the brain carries oxygen via hemoglobin. Oxygenated hemoglobin is diamagnetic such as all the other tissues but deoxygenated hemoglobin is paramagnetic causing a small, local distortion of the magnetic field. The distortions change the measurable signal that can be made visible. The technique is called *Blood Oxygen Level Dependency* (*BOLD*) imaging (see Huettel et al. 2004 for a detailed look and Forster et al. 1998 for a short tutorial).

Since brain activity is associated with the energy supply through oxygenated hemoglobin, BOLD imaging may be used to image brain activity. The ability for measuring functional activity truly differentiates MRI from CT imaging and has put MRI in competition with Nuclear Medicine Imaging techniques such as PET (described below). To produce an image from the BOLD effect, a sequence is chosen that is sensitive to local field inhomogeneities caused by the presence of deoxygenated hemoglobin. The gradient echo imaging with low angles presented in Sect. 2.2.3 is particularly sensitive to inhomogeneities and is often used in *functional MRI* (*fMRI*). It can be carried out using an EPI sequence by which an image is acquired with a single shot. Spin echo EPI can be used as well.

The BOLD effect is subtle. Reliable estimates for brain activity require experiments comprising a large number of images to cancel out noise effects. During image acquisition, a subject is asked to perform a task (e.g., listen to sound) for some time and then refrain from performing it. It is logged whether images are acquired during "action" or "no action" periods. The experiment is repeated several times. The potential correlation between intensity changes in the images and the "action"–"no action" sequence is computed for every voxel in a postprocessing phase (see Fig. 2.31).

The spatial resolution of a functional image is usually lower than that of anatomic images (128×128 voxels per slice). It may be registered with an anatomic image to relate function to anatomy.

Creating an fMRI image study is not easy. Severe distortions due to recording T_2^* images for fMRI need to be corrected properly. Motion artefacts during the study may bias the correlation of the task. Noise further reduces contrast and the resolution of the fMRI images.

Several software packages exist to register anatomic and functional images, to carry out signal analysis, and to enable intersubject studies. The most popular software, SPM, carries out statistic parametric mapping (as presented by Friston et al. (1995), webpage http://www.fil.ion.ucl.ac.uk/spm/). Other commercial as well as noncommercial alternatives exist [e.g., BrainVoyager (Goebel et al. 1998), www.brainvoyager.com, FreeSurfer (Fischl et al. 1999), surfer.nmr.mgh.harvard.edu/]. Despite the complexity of processing the functional data, fMRI is popular and currently the only technique to measure cortical activity at a spatial resolution under 3 mm. Newer scanners such as a 7T scanner, now commercially available, carry the promise of pushing the achievable resolution even further.

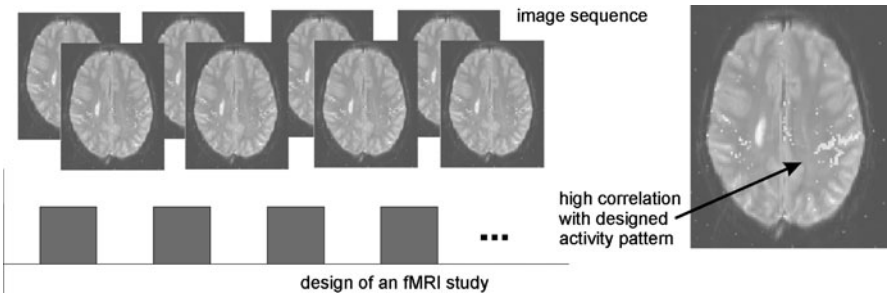

Fig. 2.31 A simple fMRI sequence consists of a sequence of images taking during a time in which a task is either on or off. Locations of which intensity changes correlate with the task design are then emphasized

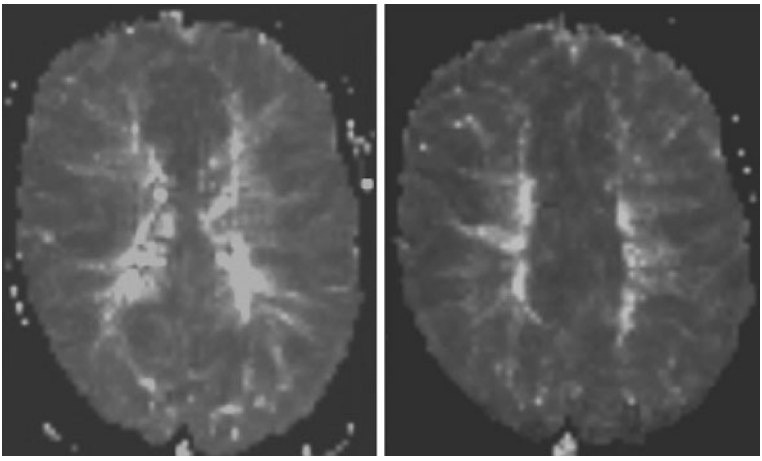

Fig. 2.32 Perfusion images are not interpreted as raw images. Diagnostically relevant measures such as the regional blood volume, regional blood flow and mean transit time are computed and visualized. The two images here show the mean transit time of two slices of the brain of a normal volunteer

2.2.7 Perfusion Imaging

Gadolinium may be used to measure *perfusion* in MRI. Gadolinium not only reduces the T_1 time, but also shortens the T_2 time (and with this the T_2^* time). The change in T_2^* is related to the amount of gadolinium. Since this is related to the amount of blood passing through the volume of tissue, gadolinium-caused T_2^* contrast predicts blood perfusion.

The main application of perfusion imaging is the depiction of parameters such as the *relative cerebral blood volume* (rCBV), relative cerebral blood flow (rCBF), and the mean transit time (MTT) in the brain (Gillard et al. 2004) (an example for the display of MTT is depicted in Fig. 2.32), perfusion imaging for tumor analysis in

the female breast (Kuhl and Schild 2000), and perfusion imaging in cardiac imaging for rest and stress studies (Jahnke et al. 2007).

For observing the primary passage of the blood bolus containing the gadolinium through the tissue, a fast sequence is needed to produce sufficient temporal resolution. Echoplanar imaging with a gradient echo sequence is one of the sequences that are fast enough and sensitive to T_2^*.

An indication for performing cerebral perfusion imaging is the diagnosis of regions affected by a stroke. Diffusion imaging (see below) can demonstrate the central effect of a stroke on the brain, whereas perfusion imaging visualizes the larger "second ring" delineating blood flow and blood volume.

2.2.8 Diffusion Imaging

Molecules in a medium are in constant motion and will stray further away from an initial start location with time. The motion is neither directed nor deterministic. After a given time it can only be said that—with certain likelihood—a molecule will be in some sphere around its initial position. The radius of the sphere depends on the time passed and on a diffusion coefficient. The latter is characteristic of the kind of molecule and the medium in which diffusion takes place. This is called *homogeneous, isotropic diffusion* and requires molecules to be able to move unhindered. Diffusion will be lower if blocked by a cell boundary. It will be anisotropic if the shape of the cell restricts diffusion in some directions more than in others.

Measuring the diffusion coefficient of isotropic diffusion is called *diffusion imaging* (Gillard et al. 2004). A change of the value of the diffusion coefficient may indicate, for instance, the breakdown of cells in the brain after a stroke. *Diffusion tensor imaging* (DTI) relates to the measurement of a tensor that describes anisotropic diffusion. A diffusion tensor $\mathbf{D}(x, y, z)$ at some voxel (x, y, z) relates the flux $\mathbf{j}(x, y, z)$ to the gradient $\mathbf{D}$ of concentration $u(x, y)$ of some diffusing quantity u in the following way:

$$\mathbf{j}(x, y, z) = -\mathbf{D}(x, y, z) \times \nabla u(x, y, z). \tag{2.13}$$

The interesting part is the tensor itself. An eigenvector decomposition of $\mathbf{D}$ will produce an orthogonal system of diffusion directions together with the variance of diffusion (the eigenvalues) in each of the directions. Elongated cells such as a nerve fiber (an axiom) should produce maximal diffusion in one of these directions. This is the direction of the fibers. Diffusion in the other two directions should be much lower (see Fig. 2.33). The knowledge of the local fiber direction is used for *fiber tracking* in the brain (Mori and van Zijl 2002), which—together with fMRI—may be used to infer the configuration of the regions of brain function (see Fig. 2.34). If two adjacent voxels belong to the same fiber bundle, they should exhibit linear diffusion and their main diffusion directions should be similar.

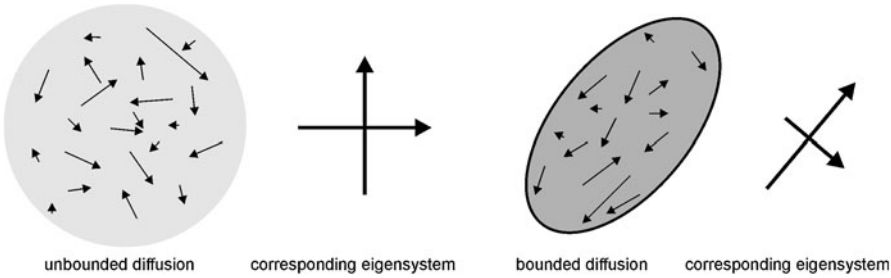

Fig. 2.33 The diffusion tensor of unbounded diffusion will have equal eigenvalues. If diffusion is bounded, eigenvalues will be lower and if the bounds are anisotropic, at least one eigenvalue will be lower than the others. Furthermore, the first eigenvector will point in the direction in which the bounded volume has its maximal extent

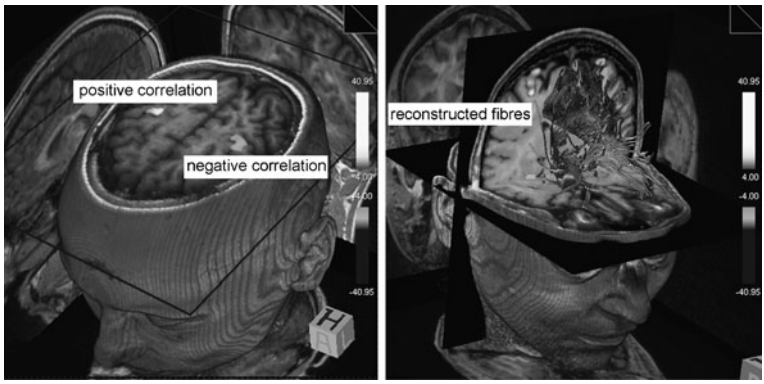

Fig. 2.34 Reconstructed fibers from diffusion MRI depicted on the right can be used with fMRI (depicted *on the left*) to infer configurations of functional regions in the brain (images from Magnetom Verio, with kind permission of Siemens Sector Healthcare, Erlangen, Germany)

Diffusion imaging by magnetic resonance employs a variant of a spin echo sequence. The purpose of the spin echo sequence is to cancel out the effects of magnetic field inhomogeneities given that the protons being imaged are static. Diffusion causes a slight loss of signal that cannot be recovered by the echo because diffusing protons move (as in phase contrast imaging). A diffusion sequence measuring isotropic diffusion emphasizes this signal loss. The amount of diffusion enhancement depends on the strength and duration of the gradient impulses and on the time between the two impulses. The diffusion coefficient can be computed if these are known.

In the case of anisotropic diffusion, the response on the gradient impulse depends on the directions of the gradient field. Elements of the diffusion tensor are computed separately by applying a sequence of different gradient excitations.

2.2.9 Image Analysis on Magnetic Resonance Images

There are a number of parallels between MRI and x-ray CT such as the reconstruction of a true 3D volume with good spatial resolution. Many analysis methods being developed for x-ray CT are, in principle, appropriate for the analysis and measurement in MR as well. There are differences, however. The much better contrast for soft tissue enables the separation of soft tissues by means of the reconstructed image intensity. However, there is no standardization of the image intensity with respect to the entity that has been measured. A T_2-weighted image may look different depending on the kind of sequence used, on the type of scanner, and on measurement parameters such as repetition time or echo time; and it certainly differs from the appearance of a T_1-weighted image. Computer-assisted analysis tools must take this into account either by incorporating scanning parameters into the method (which is seldom done), or by training the appearance from sample images, or by requesting user information at the time of analysis.

Artefacts from shading in a study with known acquisition parameters hinder defining a mapping between tissue type and image brightness within this study. The automatic separation of gray matter and white matter in the brain, for instance, which have excellent contrast in some MR images, may need to deal with the different absolute brightness of the two materials at different locations.

The wealth of different properties that can be imaged through magnetic resonance also increased interest in registration algorithms (discussed in Chap. 10). Sometimes, images showing different properties are already registered (e.g., if two echoes of a spin echo sequence are reconstructed). The first echo is dominated by proton density and the second is T_2-weighted. Clustering and classification in multidimensional feature space may, in such a case, provide further information about the entities being imaged. If registration is required (e.g., when combining functional images with a high resolution T_1-weighted image of anatomy) rigid registration is usually insufficient. Registration has to account for deformation due to the different effects of T_2^* susceptibility in different imaging sequences.

Noise in MR imaging can be a problem if an analysis tool requires the mapping of a tissue type to a small range of brightness values such as in direct volume rendering visualization or in threshold segmentation. Noise removal through the usual set of filters (to be discussed later in Chap. 4) helps, of course. It should be kept in mind, however, that most noise removal techniques operate under the hypothesis that the true image value is locally constant. Local homogeneity is not given if the size of image details reaches the limits of spatial resolution. The accidental removal of such details by noise reduction is critical in MRI since the detection of small objects is often an objective of applying MRI because of its good soft tissue contrast.

2.3 Ultrasound

Sound waves will be reflected at the boundaries between materials of different acoustic impedance. An ultrasound wave sent into the human body will be reflected at organ boundaries. The locus of reflection can be reconstructed if the speed of

Fig. 2.35 Ultrasound equipment (Siemens Acuson, with kind permission of Siemens Sector Healthcare, Erlangen, Germany)

sound in the material through which the wave travels is known (Szabo 2004). For most soft tissues this speed is around 1500 m/sec.

An ultrasound reflection signal is created using a transducer which acts as the sender and receiver of ultrasound waves (Fig. 2.35 shows typical ultrasound equipment). Frequencies for diagnostic ultrasound range between 1 and 20 MHz. High frequency waves attenuate faster than low frequency waves and do not penetrate the body as good as low frequency waves. High frequency waves resolve smaller structures, however, since the size of a reflecting object has to be larger than the wavelength.

2.3.1 Ultrasound Imaging

An ultrasound *A-scan* sends a single wave with known direction into the body and records the amplitude of reflections as a function of travel time between sending and receiving the signal. It is a one-dimensional probe into the body showing tissue boundaries and other boundaries between regions with different acoustic impedance. *Ultrasound* (*US*) *images* (the so-called *B-scans*, see Fig. 2.36) are created from a planar fan beam of differently rotated A-scans. Amplitudes are mapped to gray values for creating the image. They may also be acquired as 3D images with this fan beam rotating around a second axis perpendicular to the first axis of rotation.

Ultrasound imaging (also called *sonography*) happens in real time and is able to show the motion of the organs being imaged. Ultrasound imaging of internal organs is only possible if they are not hidden by bone since bone causes the total reflection

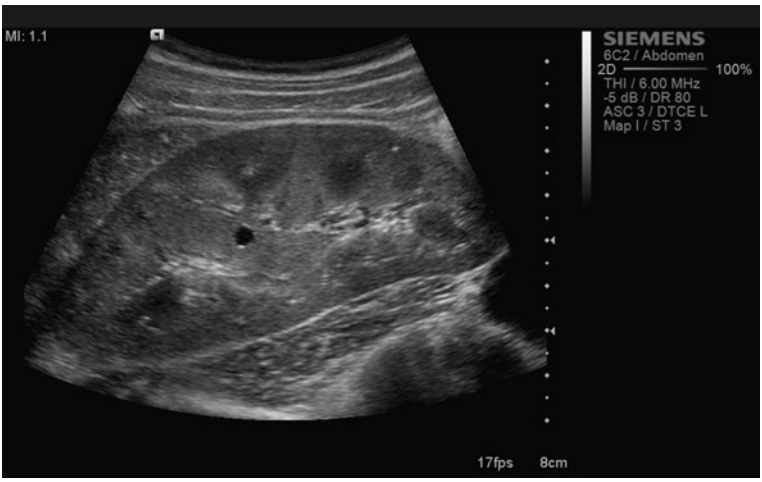

Fig. 2.36 Ultrasound B-scan of the abdomen (image with kind permission of Siemens Sector Healthcare, Erlangen, Germany)

of the incident sound waves. The organs to be imaged include the liver, gallbladder, pancreas, kidneys, spleen, heart, and uterus. Heart imaging may also be carried out by putting the ultrasound device (a transducer sending and receiving sound waves) into the esophagus.

Doppler imaging is a specific technique using the Doppler effect for estimating the speed and direction of moving objects (such as blood) in the ultrasound image (see Fig. 2.37). It is used for diagnosing the effects of vessel blockages or changes of blood flow due to stenosis.

A number of effects cause artefacts in an ultrasound image (see Fig. 2.38).

- Sound waves are attenuated just as electromagnetic waves in x-ray imaging.
- Absorption turns wave energy into heat.
- The wave may be scattered or refracted.
- Interference and a diverging wave cause further deterioration.

Absorption causes a decrease in amplitude with increasing depth. The decrease is exponential with an unknown absorption coefficient of the tissue. It is usually corrected by assuming constant absorption throughout the tissue.

Interference, scatter, and refraction of and between waves lead to the typical speckle artefacts in ultrasound images. It is a nonlinear, tissue-dependent distortion of the signal.

Tissues and tissue boundaries that reflect or attenuate a high amount of the incoming sound energy produce an acoustic shadow behind the tissue. Materials that attenuate little of the incident energy lead to signal enhancement in tissues behind this material. This is, for instance, the case when imaged organs are behind a fluid-filled organ such as a filled bladder. The smaller absorption in the fluid contradicts the hypothetically assumed constant absorption and causes a higher than necessary absorption correction.

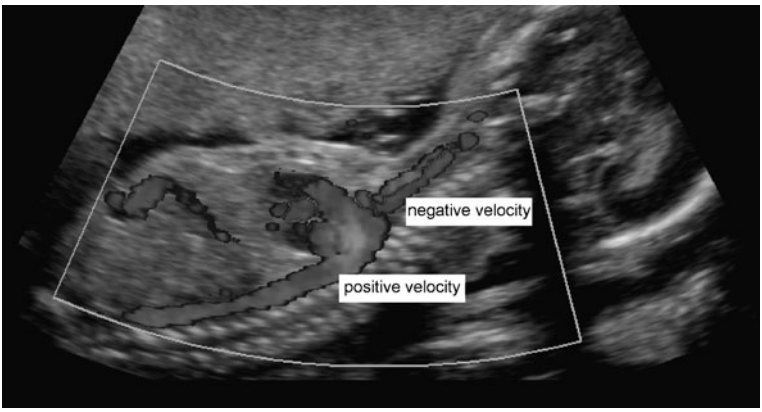

Fig. 2.37 Doppler sonography uses the Doppler effect to depict blood velocity. In its original, velocity is color-coded differentiation between flow direction and velocity (image with kind permission of Siemens Sector Healthcare, Erlangen, Germany)

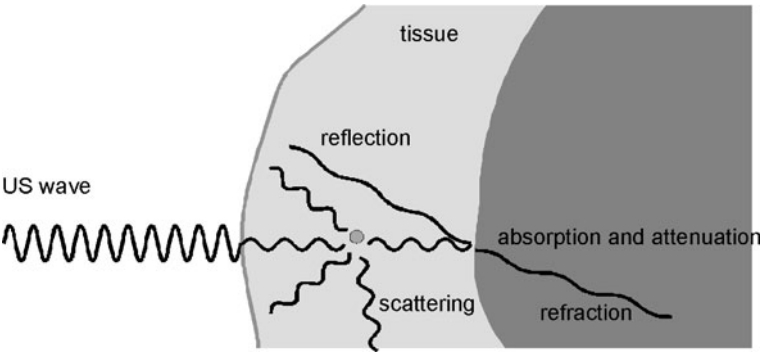

Fig. 2.38 Different effects influence the incident US wave of which only direct reflection is the wanted effect

2.3.2 Image Analysis on Ultrasound Images

Ultrasound is noninvasive and inexpensive. Hence, it is widely used as a diagnostic tool. The artefacts mentioned in the previous section as well as the approximate nature of many of the underlying assumptions for imaging may adversely influence measurements in quantitative analysis.

- Localization in ultrasound imaging assumes that the speed of sound in the material is known. It is usually taken as a constant value of the average speed of sound in soft tissue and causes signal displacement depending on the deviation from this average.
- Refraction that has not been accounted for may lead to a further displacement error.

- Organ boundaries may cause mirror echoes or multiple echoes that appear as false boundaries in the image. Mirror echoes appear behind the true boundary. Multiple echoes appear between the transducer and boundary.
- False, hyperbola-shaped boundaries may be caused by low frequency lateral oscillation of the sound wave.
- Motion artefacts lead to wave-like distortions of boundaries.
- Acoustic shadowing may hide parts of tissues and fluid-induced signal enhancement may lead to a position-dependent signal increase.
- Absorption decreases the signal-to-noise-ratio with respect to the distance from the transducer.

Artefact removal through postprocessing is only partially successful since their nonlinearity and nonstationarity defy common restoration techniques (although deconvolution in ultrasound images has been done; Jensen et al. 1993; Hokland and Kelly 1996). Using standard noise removal techniques to reduce speckle noise would seriously affect the image content since speckle is neither of high frequency nor stationary. Hence, image analysis often proceeds using the unaltered image and analysis methods have to account for this.

Tissue detection by means of their imaged intensity is impossible. However, the texture from reflection and speckle due to scatter and refraction within a tissue may be characteristic to certain tissue properties. This has been used for the texture analysis of such tissues (Wagner et al. 1985; Wu et al. 1992).

Delineation of objects in ultrasound images has to account for inexact boundary depiction due to speckle, missing signal due to acoustic shadowing, and for artefactual boundaries. Most boundary-finding algorithms therefore include some knowledge about the expected course of a boundary.

Measurements of distance, size, and angles have to account for the fact that the slice direction of the scan is operator-directed and may vary between different images of the same patient.

2.4 Nuclear Imaging

Nuclear imaging measures the distribution of a radioactive tracer material and produces images of a function in the human body. The tracer material is injected intravenously prior to the image acquisition and will distribute through blood circulation. Distribution is indicative to the perfusion of organs in the body. Examples for applications are measurements of brain activity, perfusion studies of the heart, diagnosis of inflammations due to arthritis and rheumatism, or the detection of tumor metastases due to increased blood circulation.

Images are created from measuring photons sent by the tracer material through the body. Spatial resolution in nuclear imaging is lower than for the procedures described above since tracer concentration is very low so as to not to interfere with the metabolism. The sensitivity of imaging techniques in nuclear medicine is high since detectors are able to measure a signal from a few photons. Major imaging techniques in nuclear medicine are as follows.

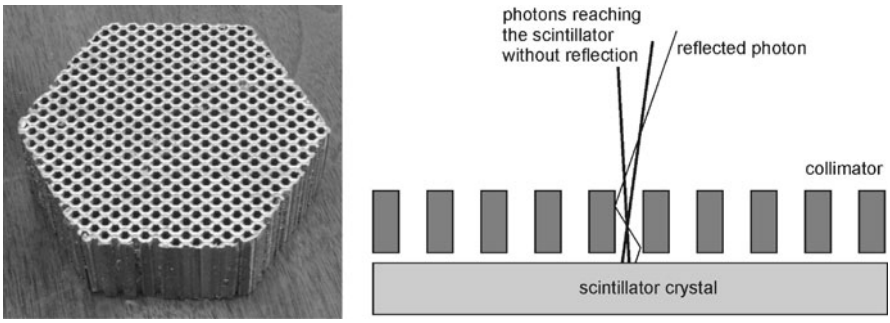

Fig. 2.39 Photons reaching the scintillator are those on (approximately) parallel rays

- *Scintigraphy*, which measures a projection of the tracer distribution with a geometry similar to projection x-ray imaging.
- *SPECT (Single Photon Emission Computed Tomography)*, which is a reconstruction from projections of tracer material producing a 3D material distribution.
- *PET (Positron Emission Tomography)*, which is a tomographic technique as well, but uses a different tracer material that produces positrons. Radiation of positron-electron annihilation is measured and reconstructed.

2.4.1 Scintigraphy

For creating a scintigram, a molecule carrying the radioactive atom $^{99\text{Tc}}$ (Technetium-99) is applied. Photons emitted by tracer radiation are measured by a *gamma camera* (also written as γ*-camera* and sometimes called *Anger camera*; see Mettler and Guiberteau 2005). The camera consists of a collimator that restricts measurements of photons to those who hit the detector approximately at a 90° angle, a *scintillator crystal* that turns incident radiation into visible light, and *photomultipliers* for amplifying the signal.

The camera is usually mounted on a gantry that enables the camera to rotate (around various directions) around the patient. The *collimator* is a thick lead plate with drilled cylindrical holes whose axes are perpendicular to the scintillator crystal. Photons reaching the detector on a path perpendicular to the detector plane will reach the scintillator at a location that is given by the positioning of the detector hole through which it passes. Photons on a path with any other angle are reflected or attenuated by the lead collimator. If they reach the detector crystal through scattering, they have lost too much energy for being detected. Hence, the collimator causes the image to be an approximate parallel projection of photons from tracer material in the body onto the image (see Fig. 2.39).

The scintigram acquired by the gamma camera is a projection of activity weighted by the attenuation that photons experience on their path between emission and detection (see Fig. 2.40 for an example). Photons are attenuated by absorption and scatter. Absorption reduces the signal while scatter reduces contrast and increases noise.

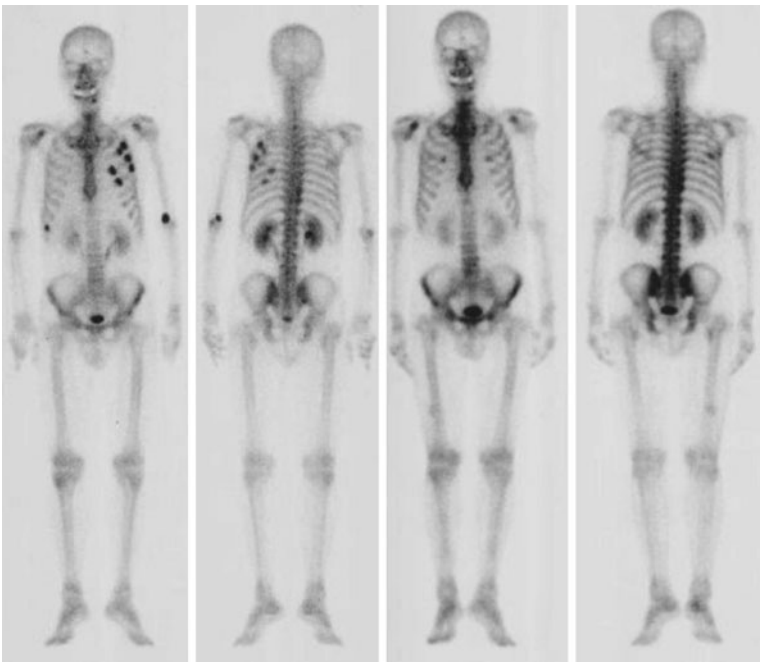

Fig. 2.40 Bone scintigraphy (in this case before and after-treatment bone scintigraphy from Mado et al. 2006, published under Creative Commons license)

Collimator characteristics limit spatial resolution and contrast of the scintigram (see Fig. 2.41). Photons reaching the detector do not exactly follow a path perpendicular to the detector plane. They originate from a cone-shaped volume whose size is determined by the diameter and the length of the cylindrical apertures in the collimator. Reducing the diameter and increasing the length will increase the spatial resolution, but it will also decrease the number of photons that reach the scintillator crystal, hence reducing the signal.

2.4.2 Reconstruction Techniques for Tomography in Nuclear Imaging

Slice computation from multiple views of the gamma camera is done by applying tomographic reconstruction techniques. A sequence of images is acquired while the gamma camera rotates around the patient. If the axis, around which the camera rotates, is taken as the y-axis of a device coordinate system, a slice may be reconstructed from lines with a constant x-value of all projection images made by the camera.

Slice reconstruction of nuclear images from projections for SPECT and PET is similar to reconstruction from x-ray projection but with an important difference, which makes the FBP technique of x-ray CT less suitable for slice reconstruction

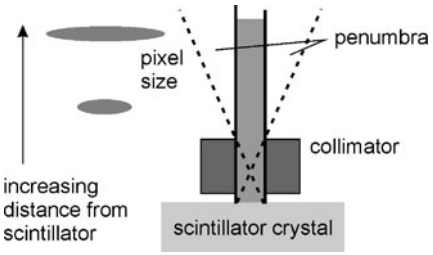

Fig. 2.41 The geometry of the collimator limits the spatial resolution of the scinitgram. Resolution decreases with distance to the gamma camera

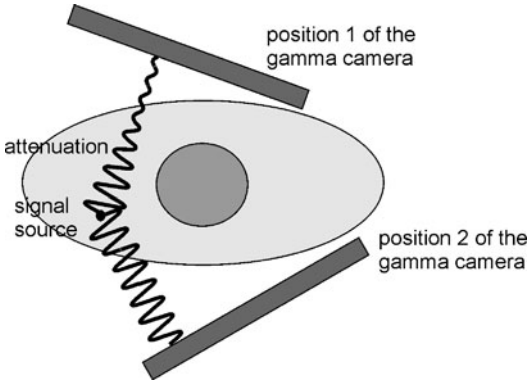

Fig. 2.42 Attenuation that depends on the attenuation coefficients along the path between emission site and detector causes different activity levels to be measured of from the same site if the detection position is different

although it is commonly used in commercial software. The aim of reconstruction is to depict the spatial distribution $\mu(x, y)$ of radioactive tracer material. Reconstruction from projection would require projection of this distribution. The measurement, however, consists of projected, *attenuated* activity. Attenuation depends on the material between the emission site and detector. This violates the assumption of the Radon transform since the contribution of $\mu(x, y)$ to a line integral is dependent on the projection direction (see Fig. 2.42).

If attenuation is neglected, filtered backprojection may be used. However, it may lead to signal degradation, which is unwanted in view of the already low signal. If attenuation were known for each voxel (x, y) in any projection direction (θ, s), it could be accounted for, provided a suitable reconstruction algorithm exists.

Such a technique is given by modeling reconstruction as a problem of estimating unknowns (the unknown densities $\mu(x, y)$) from a number of (linear) equations, which are the different projections. The oldest method based on this model, which originally was also used to reconstruct CT images, is the *algebraic reconstruction technique* (ART; Herman et al. 1978). For reconstructing the image, variables are rearranged so that all unknown densities μ are in a 1D vector $\mathbf{x}$. Projections are arranged in another 1D vector $\mathbf{y}$ (see Fig. 2.43). Now, the reconstruction requires finding an $\mathbf{x}$, for which

$$\mathbf{Mx} = \mathbf{y}. \tag{2.14}$$

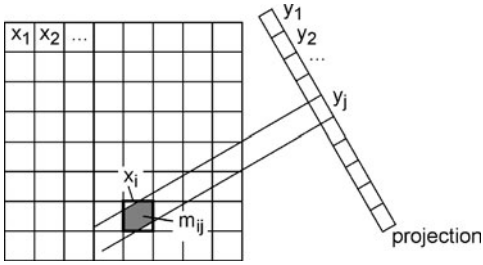

Fig. 2.43 Projection geometry for algebraic reconstruction. The value of m_{ij} is the ratio of the total area of pixel x_i that is covered by ray y_j

Elements m_{ij} of matrix $\mathbf{M}$ contain weights that represent how much of the volume in element x_i is measured in the projection y_j ($m_{ij} = 0$, if the projection ray y_j does not pass x_i; otherwise it is the relative volume of the voxel x_i, which is covered by a cylindrical ray y_j).

The matrix $\mathbf{M}$ can be very large and it is not necessarily square. If an image with 256×256 elements shall be reconstructed from 180×350 projections, the matrix would have $65{,}536 \times 63{,}000$ elements. Even if it were a square matrix it may be singular. The reconstruction is done numerically in an iterative fashion.

The reconstruction scheme is simple. Suppose that an estimate $\mathbf{x}^{(n)}$ of $\mathbf{x}$ is given. Then, an estimate $\mathbf{y}^{(n)} = \mathbf{M}\mathbf{x}^{(n)}$ of the projection vector can be computed. This estimate is compared with the true projection $\mathbf{y}$. The error $y_j - y_j^{(n)}$ for some projection y_j is then used to correct the equation $y_j = \sum_{j=0}^{N} m_{ij} x_j$ in the following way:

$$x_i^{(n+1)} = x_i^{(n)} + \left(y_j - y_j^{(n)}\right) \frac{m_{ij}}{\sum_{i=0}^{M} m_{ij}}. \tag{2.15}$$

This procedure is repeated for every equation in the system and—since corrections of $\mathbf{x}$ from a later equation will have changed earlier corrections—it will be iterated until the residual error $\|\mathbf{y} - \mathbf{y}^{(n)}\|$ falls below some threshold. The first estimate $\mathbf{x}^{(0)}$ can be simply $\mathbf{x}^{(0)} = \mathbf{0}$ or it may be an estimate from some other reconstruction technique (e.g., FBP).

Algebraic reconstruction takes much longer than FBP and is no longer applied for CT reconstruction. However, it is particularly easy to include effects such as attenuation into the problem. If α_{ij} is the attenuation of photons emitted at x_i and detected at y_j, all that is needed is to weight the m_{ij} (which may be interpreted as the likelihood of an emitted photon at x_i to be detected at y_j) with α_{ij}.

Reconstruction in SPECT and in PET employs this strategy although a different reconstruction strategy is used. Photon detection is treated as a random process with known probability distribution. The method is called *maximum likelihood expectation maximization* (*MLEM*) *reconstruction*. For a detailed treatment see Lange and Carson (1984) for an introductory treatment of common reconstruction techniques in nuclear imaging.

To model the problem, we assume that photon emission is a random process and that x_i is the mean number of photons emitted at location i, which is detected at location y_j with probability m_{ij}. It results in the same equation as above, but

with a slightly different meaning for $\mathbf{x}$ and $\mathbf{y}$. The number of photons detected at j depends on the probability that it is attenuated on its way, which in turn depends on the density, i.e., the mean number of photons $\bar{y}_j$ along the ray, which is

$$\bar{y}_j = \sum_{i=1}^{M} m_{ij} x_i . \tag{2.16}$$

It can be described by a Poisson process, whereby the probability of detecting y_j photons at j is

$$P(y_j) = \frac{\exp(-\bar{y}_j) \cdot (\bar{y}_j)^{y_j}}{y_j!}. \tag{2.17}$$

The measurements and thus the probabilities are independent. The conditional probability $P(\mathbf{y}|\mathbf{x})$ of observing measurement $\mathbf{y}$ given the tracer distribution $\mathbf{x}$ is the product

$$L(\mathbf{x}) = P(\mathbf{y}\,|\bar{\mathbf{x}}) = \prod_{j=1}^{N} P(y_j) = \prod_{j=1}^{N} \frac{\exp(-\bar{y}_j) \cdot (\bar{y}_j)^{y_j}}{y_j!}. \tag{2.18}$$

The maximum of L is computed by taking the derivative and setting it to zero. To simplify the computation, the derivative is taken on the log-likelihood (maximizing the logarithm l of L also maximizes L)

$$l(\mathbf{x}) = \sum_{j=1}^{N} -\bar{y}_j + y_j \ln(\bar{y}_j) - \ln(y_j!). \tag{2.19}$$

Replacing $\bar{y}_j$ by the right-hand side of (2.16), we get

$$l\,(\mathbf{x}) = \sum_{j=1}^{N} \left(-\sum_{i=1}^{M} m_{ij} x_i + y_j \ln \left(\sum_{i=1}^{M} m_{ij} x_i \right) - \ln(y_j!) \right). \tag{2.20}$$

Taking the partial derivatives with respect to the x_i (using the chain rule and remembering that the derivative of $\ln x$ is $1/x$), we get

$$\frac{\partial l(\mathbf{x})}{\partial x_i} = -\sum_{i=1}^{M} m_{ij} + \sum_{j=1}^{N} \frac{y_j}{\sum_{i=1}^{M} m_{ij} \bar{x}_i} m_{ij} x_i = 0. \tag{2.21}$$

Multiplying both sides with x_i and resolving for x_i, we receive

$$x_i = -\frac{x_i}{\sum_{i=1}^{M} m_{ij}} \cdot \sum_{j=1}^{N} \frac{y_j}{\sum_{i=1}^{M} m_{ij} \bar{x}_i} m_{ij}, \tag{2.22}$$

which can be turned into the iteration step

$$x_i^{(n+1)} = -\frac{x_i^{(n)}}{\sum_{i=1}^{M} m_{ij}} \cdot \sum_{j=1}^{N} \frac{y_j}{\sum_{i=1}^{M} m_{ij} \bar{x}_i^{(n)}} m_{ij}. \tag{2.23}$$

This is the MLEM algorithm. Again, *attenuation correction* may be added by modifying the likelihoods m_{ij} with the attenuation weight. Other effects such as the loss of resolution with distance to the detector can be included in the weighting as well. Even scatter interaction can be included although this is not possible by simply adopting the weighting since interactions between sites have to be modeled (Shcherbinin et al. 2008).

A variant of the MLEM algorithm is *OSEM* (*ordered subset expectation maximization*), by which the order in which equations are updated is changed (Hudson and Larkin 1994). If projections are taken from 96 angles, projection angles may be ordered in, say, 16 subsets with projections 1, 17, 33, ..., in the first subset, projections 2, 18, 34, ..., in the second subset and so on. This reconstruction strategy has been shown to speed up convergence. The factor by which convergence increases is in the order of numbers of subsets.

Image reconstruction with EM increases noise in later iterations because noise characteristics are not accounted for. This means that it can be difficult to decide when to stop the algorithm. *MAP-EM* (*maximum a posteriori expectation maximization*) remedies this by including *a priori* knowledge about desired smoothness in the model. Different versions of MAP-EM exist. They have in common that smoothness is described by making constraints about activity differences in adjacent pixels. An algorithm by Green (1990), which is called the *OSL* (*one-step-late*) algorithm, for computing the MAP-EM estimate is similar to the EM algorithm. The term $\sum_{i=1}^{M} m_{ij}$ in (2.23) is replaced by

$$\sum_{i=1}^{M} m_{ij} + \beta \frac{\partial}{\partial x_i} U\left(\bar{x}_i^{(n)}\right), \tag{2.24}$$

where $\frac{\partial}{\partial x_i} U(\bar{x}_i^{(n)})$ is an energy term enforcing smoothness, e.g.,

$$\frac{\partial}{\partial x_i} U\left(\bar{x}_i^{(n)}\right) = \sum_{k \in Nbs(i)} w_{ik}\left(\bar{x}_i^{(n)} - \bar{x}_k^{(n)}\right), \tag{2.25}$$

and $Nbs()$ refers to some neighborhood around a site i. The weighting term w_{ik} balances different types of neighboring pixels (e.g., neighbors at different distances).

Fig. 2.44 Two-plane SPECT imaging system used in cardiac imaging (with kind permission from Siemens Sector Healthcare, Erlangen, Germany)

2.4.3 Single Photon Emission Computed Tomography (SPECT)

SPECT uses projection images from the gamma camera to create an image of the radioactive tracer distribution (Mettler and Guiberteau 2005) (see Fig. 2.44 for an example of the image acquisition system used in cardiac SPECT). Images without attenuation correction can be reconstructed by FBP yielding a spatial resolution of approximately 3 to 6 mm side length of a pixel. Image sizes vary between 64 × 64 and 128 × 128 voxels per slice with 25 to 35 slices to be reconstructed. Using iterative reconstruction, attenuation correction and smoothness constraints may be included, leading to a better image quality at the expense of longer reconstruction times if compared to FBP (see Fig. 2.45). Attenuation maps can be generated from the reconstruction of a transmission scan taken prior to imaging.

The acquisition of SPECT images can be carried out by a single rotating gamma camera. However, modern systems use *3-head cameras* for capturing three projections at a time. The acquisition time for a single projection is about 15 to 20 seconds, which amounts, for a 3-head system, to total acquisition times between 5 and 10 minutes.

Scatter in SPECT decreases contrast and causes noise in the image. Due to the small number of photons measured, scatter may also cause artefacts since scattering in dense materials with a high uptake of radioactive material may be falsely attributed to nearby regions. Scattered photons due to Compton scattering can be identified due to the energy loss of the scattered photon. Scattered photons may be

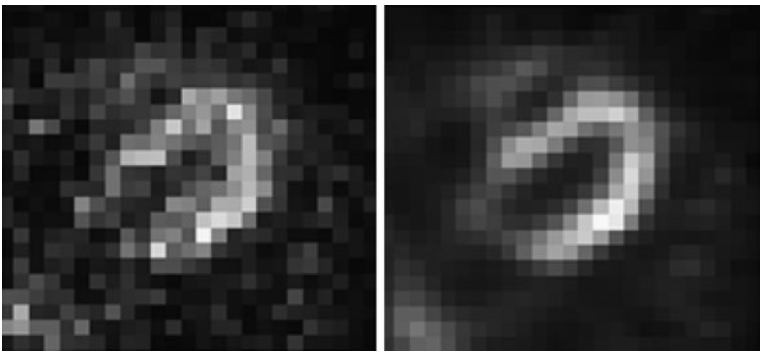

Fig. 2.45 SPECT image of the left ventricle. The two images are not smoothed in order to reveal their true spatial resolution. The *left image* was reconstructed without, the *image on the right* with attenuation correction using the method of Celler et al. (2005) (with kind permission of Anna Celler, Department of Radiology, University of British Columbia, Vancouver)

removed by the appropriate frequency filtering of the signal. The removal of scatter does reduce artefacts, but it cannot increase the signal-to-noise-ratio.

Artefacts due to motion during image acquisition cause blurring of the data. Non-gated cardiac SPECT is not able to show the heart motion because of the long acquisition time, but produces an average image over the complete heart cycle.

Major application fields for SPECT imaging are the imaging of ventricular perfusion and ejection fraction of the heart, scans of lungs, kidneys, liver, and bone for tumor detection, and brain perfusion studies.

2.4.4 Positron Emission Tomography (PET)

PET uses positron emitters for producing the image (Mettler and Guiberteau 2005). Radioactive isotopes of atoms such as oxygen or fluoride emitting positrons are administered to the human body. If distributed in the body, emanating positrons annihilate if they meet an electron and produce two photons that are emitted in the near-opposite direction. Photon energy is 511 keV. Events are measured by a *detector ring* and do not require collimators. An annihilation event is registered if two photons are detected at nearly the same time (within nanoseconds). The event is attributed to a location on a line connecting the two detection sites (see Fig. 2.46). This line is called the *line of response (LOR)*.

PET is an expensive technique if compared to SPECT because positron emitting isotopes have a short half-life and need to be generated in a cyclotron in close neighborhood to the PET scanner. The scanning technique is demanding, requiring a fixed detector ring that is capable of analyzing events according to synchronicity of measurement. The image quality of PET is better than SPECT. The number of attenuated photons decreases without collimation, the higher energy of the photons reduces attenuation loss in the body, and the near-parallelism of the path of the two

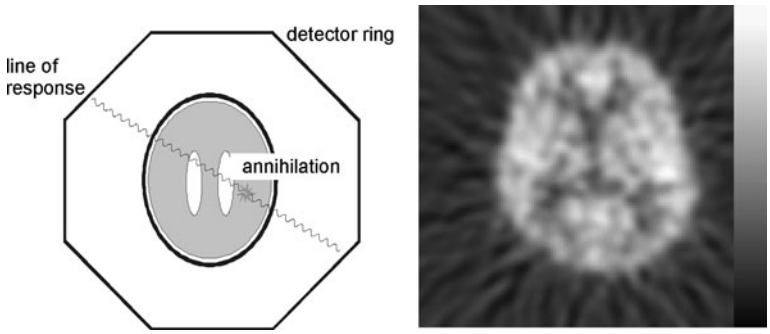

Fig. 2.46 Schematic view of a PET scanner (*left*) and resulting image of measured activity in the brain

protons focuses the ray better than the cylindrical aperture of the collimator in a gamma camera.

The spatial resolution of PET is in the range of 2 to 5 mm side length of a voxel. The signal-to-noise level is low due to the low number of counts. The true spatial resolution (i.e., the closest distance between two discernable objects) is often sacrificed to reduce noise by smoothing the data during or after reconstruction. PET, similarly to SPECT, does not produce anatomic information. Metabolic function as imaged by PET is best evaluated if registered with some anatomic scan (e.g., from CT or MRI). Registration algorithms for the registration of PET with anatomic imagery were developed in the 1980s and 1990s (Pelizzari et al. 1989). The technical problems of registration at the resolution of PET images can be considered to be solved. Some of today's PET machines are combined with a multislice CT scanner for creating anatomic and functional images almost simultaneously and in close registration.

One of the many uses of functional imaging using PET is to observe brain activity using an oxygen isotope as a tracer. Being able to resolve cortex activity at resolutions of 5 to 10 mm stipulated much activity beginning in the late 1980s because PET, for the first time, allowed to observe activity at a resolution that is comparable to the size of major substructures—such as the visual cortex—in the brain (Senda et al. 2002). Presently, functional brain imaging through PET is challenged by fMRI, which is able to measure activity at an even higher spatial resolution than PET although being only an indirect indicator using the BOLD effect.

Further applications for PET imaging are the analysis of tumor metabolism in oncology or the tracing of labeled neuroreceptors in psychiatry.

2.4.5 Image Analysis on Nuclear Images

Images come as projection images as well as slice images sharing the advantages and disadvantages of such kinds of images, as explained in the section on computed tomography. The signal strength in the images depends on the amount of tracer given

and the individual metabolism. Quantitative measurements based on intensity are usually a comparison of activity between two regions because the absolute intensity value at some location depends on external factors.

The image quality (i.e., resolution and signal-to-noise ratio) is poor because of the low number of photons contributing to an image and because of the restrictions from image acquisition. This sometimes requires integrating quantitative measurements of relative activity over a larger region for arriving at reliable estimates.

Analysis often requires correlating the functional signal with anatomy. One should never be tempted to take the apparent agreement between activity distribution and expected anatomy as reason to derive anatomy from the functional signal. Anatomy and function may coincide, but a major purpose using a nuclear imaging technique is to identify and analyze regions where this is not the case. If analysis has to be carried out with respect to anatomy (e.g., "which part of the cardiac ventricle in a SPECT image is perfused normally?"), anatomical information has to be supplied by other means such as registering the data with anatomic images or an anatomic model of the organ to be imaged.

2.5 Other Imaging Techniques

The image modalities discussed so far make up the majority of images that are subjected to computer-assisted analysis. We will conclude this chapter with a brief discussion of some other methods that—although in part quite common in clinical practice—are not often subject to image analysis methods. The reasons for this are that, at present, most of them are diagnosed quite satisfactorily by inspection by a human expert.

2.5.1 Photography

An example for diagnosis using photography is the depiction of vascular processes in retina photography (see Fig. 2.47). The retina is the only location in the human body where vessels are visible on the surface (Saine and Tyler 2002). Another application is the diagnosis and staging of skin tumors (Malvehy 2002) or burn scars (van Zuijlen et al. 2002). Photography in this field is sometimes replaced by dermoscopy (Bowling 2011) which produces microscopic images of the skin surface with a magnification factor of 1:10.

In treatment planning, photography may be used for estimating the effects of plastic surgery. Digital photographs are usually high quality and high resolution color images.

A photographic image is a projection of some opaque surface, so that similar rules with respect to measurement and analysis apply than for x-ray projection images. If, for instance, distances on the retina surface shall be measured, the curvedness of the retina and the magnification factor due to the distance between the camera and retina has to be considered. When using intensity or color in digital pho-

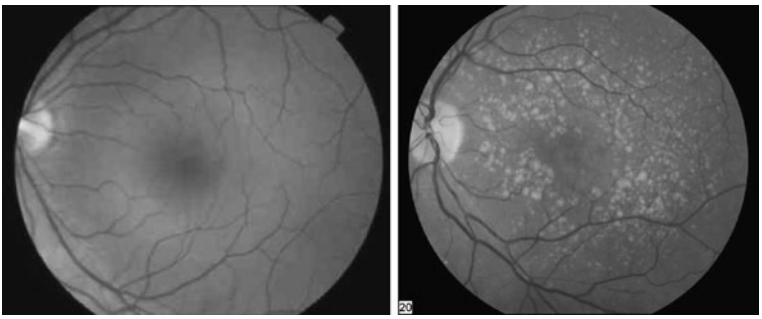

(a) (b)

Fig. 2.47 Examples of retina photography (note that the original images are in color): (**a**) retina of a normal (**b**) degeneration of the macula (with kind permission of the National Eye Institute http://www.nei.nih.gov)

tographs for analysis, effects from external lighting, shading, or the camera position need to be accounted for.

2.5.2 Light Microscopy

Microscopes in medical imaging are often light-optical microscopes, which are able to analyze living structures of sizes between 0.1 µm and 1 mm. Magnification is generated through a system of lenses. Photosensitivity decreases with increased spatial resolution. Microscopic images are often used for the diagnosis of pathology in a tissue specimen on the cell level (see, e.g., Fig. 2.48). Images are usually color images with good contrast and signal-to-noise ratio. Microscopic images are used for cell counting, shape analysis of cells, and structural analysis of cells and cell distribution (Török and Kao 2008).

Microscopic images are good quality high resolution images, which may suffer from blurring due to defocussing. Since color staining in cells is done on purpose, color-based segmentation and classification are often appropriate strategies for successful analysis. Cell classification and the detection of the structural arrangement of cells may require quite elaborate segmentation techniques and a very good understanding of the often qualitative criteria to categorize cells.

A variant of cell microscopy is fluorescence microscopy. Instead of using reflection and absorption, the signal is generated by the fluorescence response of the living material to incident laser light. Since the response is at a different wavelength than the evoking laser light, influences from light reflection and absorption can be filtered so that the image only shows the fluorescence of the reacting material (Fig. 2.49 shows examples of fluorescence microscopy of the synaptic vesicles from drosophila larvae).

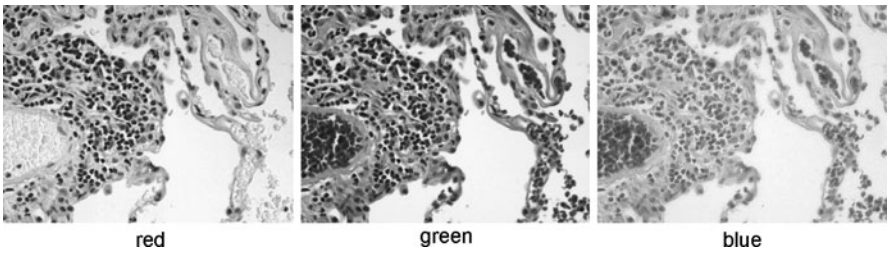

Fig. 2.48 Red-, green- and blue-channel of a color-stained microscopic image of lung cells (image taken from Rogers 2004 published under Creative Commons license)

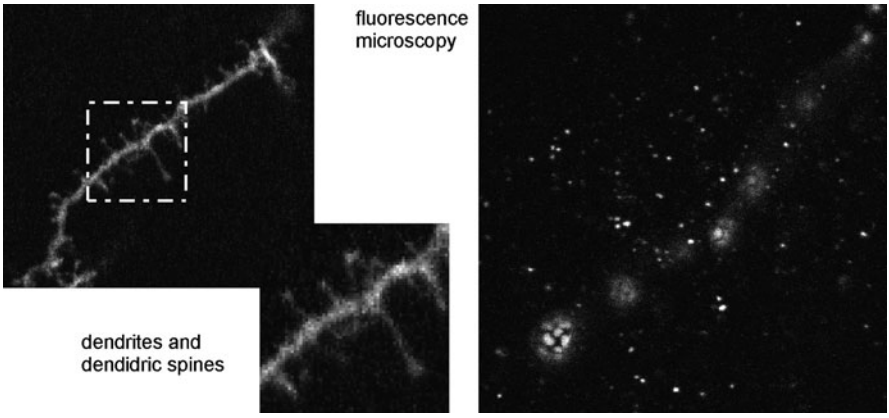

Fig. 2.49 Dendritic spine (*left*) and fluorescence microscopy (*right*) of the synapses of drosophila larvae, see Bachmann et al. (2004). It is characteristic for fluorescence images that only fluorescent particles are visible while influence from the incident illumination is filtered out (the original images are in color showing different types of particles in different color channels). Hence, the dendrite is not visible in the *image on the right*

2.5.3 EEG and MEG

For creating an *electroencephalogram* (*EEG*) a number of electrodes (16 to 25) are placed on the scalp to detect electrical impulses caused by brain activity. The impulses are amplified and represent an array of brain activity curves indicating the function of the human brain. Brain activity happens in gray matter, which—for the most part—is close to the scalp. Hence, EEG provides a brain map of functional activity (Chambers and Sanei 2007).

Spatial resolution is poor, but the temporal resolution of EEG is excellent (see Fig. 2.50 for an example of EEG time curves). Hence, EEG is a potential candidate to supplement methods with good spatial resolution and low temporal resolution of imaging (such as fMRI). An EEG measures neural activity directly whereas other methods such as fMRI, SPECT, or PET deduce brain activity from secondary signals (such as the blood oxygen level). Currently, the main activity in processing EEGs is

Fig. 2.50 An EEG consists of a set of time signals that are acquired from different locations on the head surface. Lines of the original EEG were dilated in this picture for enhanced visibility (EEG entry of www.wikipedia.de from user "Der Lange", published under Creative Commons license)

signal analysis and pattern recognition of the temporal image. Image analysis plays a lesser role due to the poor spatial resolution of the signal.

A *magnetoencephalogram* (*MEG*) measures a similar effect as EEG through the magnetic field of neural brain activity (Hämäläinen et al. 1993; Papanicolaou 1995). MEG requires a system for recording very small magnetic fields (10^{-15} T) and requires a special kind of recording magnet that is sensitive to such small fields (it is called *SQUID—superconducting quantum interference device*). Measuring a magnetic field that is more than a billion times smaller than the Earth's magnetic field requires excellent shielding of the examination room. Compared to EEG, requirements for applying MEG are much higher. However, the achievable spatial resolution of about 2 mm is much better than in EEG. The temporal resolution is 1 ms and in the same range as EEG.

MEG is a very new technique and does not produce images yet. Hence, not much can be said about its potential and of the properties of such images. So far, spatially resolved MEG was mainly used for the exact localization of a certain activity. However, acquiring a surface map of the cortex is possible in principle and may provide excellent spatiotemporal resolution.

2.6 Concluding Remarks

Image acquisition methods presented in this chapter can be grouped by acquisition technique into projective and nonprojective methods, by the imaged parameters into physiological and functional imaging techniques, and by the physical effect that is

measured. Each of the techniques produces information that is related to physiological and/or functional attributes in a known way. It can be assumed that the selection of an imaging technique is always intentional so that this relation can be exploited for subsequent analysis. Artefacts are often specific to an imaging technique so that this knowledge can and should be used when developing an analysis method.

The term "medical image" comprises a wide variety of different acquisition techniques and different signals to be acquired. Hence, understanding the semantics of the image will require a new effort every time that a new analysis task shall be solved with the help of a semi-automatically or automatically working algorithm. This is one of the major differences between processing medical images and other pictures. Another important aspect is that the depiction is usually not the projection of mostly opaque materials, but either a projection of transparent materials (such as in x-ray imaging or in scintigraphy) or a full reconstruction of a 3D (or even 4D) scene. Recovery of distances or the treatment of partially hidden structures being in the focus of many computer vision algorithms are therefore not a major concern of the analysis of medical images. The main problems in medical image analysis are to deal with the incomplete differentiation of structures of interest, with artefacts from image acquisition and with the inaccessibility of the data to be analyzed.

2.7 Exercises

- Why is it impossible to measure distances in projections images?
- Why is angiography in cardiac imaging more popular than digital subtraction angiography?
- Explain the difference of the imaging technique between standard x-ray imaging and mammography.
- Explain the image acquisition process for digital radiography.
- What is meant by vignetting in radiographic imaging and what are the effects of this artefact?
- What is the partial volume effect and how does it affect the image?
- Why is it necessary to filter the projection data in filtered backprojection?
- Explain the backprojection procedure.
- What is the major difference between CT angiography and 3D reconstructed digital subtraction angiography?
- What is the purpose of filtering with a Hamming window filter when reconstructing CT images?
- What is meant by window and level in displaying CT images? Why is it needed?
- What is the typical spatial resolution of a body CT scan?
- Name three typical artefacts that occur in CT and MR imaging.
- What is the entity in the body that gives rise to the signal in MR imaging?
- Explain the meaning of the three components (ρ, t_1, t_2) that make up the MR signal.
- Explain the steps of slice selection, phase, and frequency encoding in MR imaging.

- What is the difference between t_2-relaxation and t_2^*-relaxation in MR imaging?
- How does the spin-echo sequence in MR imaging avoid adverse effects from t_2^*-relaxation?
- Why is most MR image acquisition much slower than CT image acquisition?
- What is the principle of fast MR imaging techniques such as EPI imaging?
- Name and explain the differences between the different kinds of angiogtaphic imaging in MRI. Which of the techniques can be used to recover velocity information?
- What is meant by ghosting in MR imaging and when does it occur?
- What imaging technique uses Hounsfield units for normalization and what are the two reference values for normalization?
- What is the purpose of MR perfusion imaging? How is the perfusion information generated?
- What is the BOLD effect and how is it used in functional MRI?
- Why is it necessary to acquire a time sequence of images in functional MRI?
- What is measured in diffusion imaging? Why and how can this information be used for fiber tracking?
- What are A- and B-scans in ultrasound imaging?
- How is spatial information about the depth of a reflection generated in ultrasound imaging?
- Name some typical artefacts in ultrasound images.
- What imaging techniques are subsumed under the term "nuclear imaging"? Which of the techniques produces projection images?
- Explain the design of a gamma camera. What is the purpose of the collimator in this design?
- What are the adverse influences for reconstructing SPECT images?
- What are the reasons for SPECT having a low spatial resolution compared to, e.g., CT imaging?
- What are potential diagnostic questions that require a scintigraphy?
- What are the advantages and disadvantage of MRI opposed to x-ray CT?
- Why is filtered backprojection not always appropriate to reconstruct SPECT images?
- Why is the spatial resolution of PET generally higher than the one of SPECT?
- What generates the signal in PET imaging? How does PET compare with functional MRI?
- What are the applications for using photography in diagnosis?
- What are the potential applications of using light microscopy?
- What is measured by an EEG? What is the spatial resolution of the signal?
- Name a potential application for acquiring an EEG?
- What other imaging techniques produce similar information as that generated by EEG?

References

Akpek S, Brunner T, Benndorf G, Strother C (2005) Three-dimensional imaging and cone beam volume CT in C-arm angiography with flat panel detector. Diagn Intervent Radiol 11:10–13

Bacher K, Smeets P, Bonnarens K, De Hauwere A, Verstraete K, Thierens H (2003) Dose reduction in patients undergoing chest imaging: digital amorphous silicon flat-panel detector radiography versus conventional film-screen radiography and phosphor-based computed radiography. Am J Radiol 181:923–929

Bachmann A, Timmer M, Sierralta J, Pietrini G, Gundelfinger ED, Knust E, Thomas U (2004) Cell type-specific recruitment of Drosophila Lin-7 to distinct MAGUK-based protein complexes defines novel roles for Sdt and Dlg-S97. J Cell Sci 117(10):1899–1909

Bowling J (2011) Diagnostic dermoscopy: the illustrated guide. Wiley, New York

Bushberg JT (1998) X-ray interaction. Radiographics 18(2):457–468

Bushberg JT, Seibert JA, Leidholdt EM (2002) The essential physics of medical imaging, 2nd edn. Lippincott Williams and Wilkins, Philadelphia

Buzug TM (2008) Computed tomography—from photon statistics to modern cone-beam CT. Springer, Berlin

Celler A, Dixon KL, Chang Z, Blinder S, Powe J, Harrop R (2005) Problems created in attenuation-corrected SPECT images by artefacts in attenuation maps: a simulation study. J Nucl Med 46(2):335–343

Chambers JA, Sanei S (2007) EEG signal processing. Wiley, New York

Chan HP, Doi K, Galhotra S, Vyborny CJ, MacMahon H, Jokich PM (1987) Image feature analysis and computer-aided diagnosis in digital radiography. I. Automated detection of microcalcifications in mammography. Med Phys 14(4):538–548

Cheng HD, Lui YM, Freimanis RI (1998) A novel approach to microcalcification detection using fuzzy logic technique. IEEE Trans Med Imaging 17(3):442–450

Dengler J, Behrens S, Desaga JF (1993) Segmentation of microcalcifications in mammograms. IEEE Trans Med Imaging 12(4):634–642

Dillon EH, van Leeuwen MS, Fernandez MA, Mali WP (1993) Spiral CT angiography. Am J Roentgenol 160(6):1273–1278

Dumoulin CL (1995) Phase contrast MR angiography techniques. Magn Reson Imaging Clin N Am 3(3):399–411

Fink C, Hallscheidt PJ, Noeldge G, Kampschulte A, Radeleff B, Hosch WP, Kauffmann GW, Hansmann J (2002) Clinical comparative study with a large-area amorphous silicon flat-panel detector—image quality and visibility of anatomic structures on chest radiography. Am J Radiol 178:481–486

Fischl B, Sereno MI, Dale AM (1999) Cortical surface-based analysis. II. Inflation, flattening, and a surface-based coordinate system. Neuroimage 9:195–207

Forster BB, MacKay AL, Whittall KP, Kiehl KA, Smith AM, Hare RD, Liddle PF (1998) Functional magnetic resonance imaging: the basics of blood-oxygen-level dependent (BOLD) imaging. Can Assoc Radiol J 49(5):320–329

Friston KJ, Holmes AP, Worsley KJ, Poline JP, Frith CD, Frackowiak RSJ (1995) Statistical parametric maps in functional imaging: a general linear approach. Hum Brain Mapp 2(4):189–210

Garmer M, Hennigs SP, Jäger HJ, Schrick F, van de Loo T, Jacobs A, Hanusch A, Christmann A, Mathias K (2000) Digital radiography versus conventional radiography in chest imaging—diagnostic performance of a large-area silicon flat-panel detector in a clinical CT-controlled study. Am J Radiol 174:75–80

Geluk RJ (1979) Transverse analogue tomography (TAT): a new method for cross-sectional imaging using X-rays. J Mod Opt 26(11):1367–1376

Ghersin E, Litmanovich D, Dragu R et al (2006) 16-MDCT coronary angiography versus invasive coronary angiography in acute chest pain syndrome: a blinded prospective study. Am J Roentgenol 186(1):177–184

Gillard JH, Waldman AD, Barker PB (2004) Clinical MR neuroimaging: diffusion, perfusion and spectroscopy. Cambridge University Press, Cambridge

Goebel R, Sefat DK, Muckli L, Hacker H, Singer W (1998) The constructive nature of vision: direct evidence from functional magnetic resonance imaging studies of apparent motion and motion imagery. Eur J Neurosci 10(5):1563–1573
Green PJ (1990) Bayesian reconstructions from emission tomography data using a modified EM algorithm. IEEE Trans Med Imaging 9(1):84–93
Hämäläinen M, Hari R, Ilmoniemi RJ, Knuutila J, Lounasmaa OV (1993) Magnetoencephalography—theory, instrumentation, and applications to noninvasive studies of the working human brain. Rev Mod Phys 65(2):413–497
Herman GT, Lent A, Lutz PH (1978) Relaxation methods for image reconstruction. Commun ACM 21(2):152–158
Hokland JH, Kelly PA (1996) Markov models of specular and diffuse scattering in restoration of medical ultrasound images. IEEE Trans Ultrason Ferroelectr Freq Control 43(4):660–669
Hudson HM, Larkin RS (1994) Accelerated image reconstruction using ordered subsets of projection data. IEEE Trans Med Imaging 13(4):601–609
Huettel SA, Song AW, McCarthy G (2004) Functional magnetic resonance imaging. Palgrave Macmillan, Basingstoke
Jahnke C, Nagel E, Gebker R, Kokocinski T, Kelle S, Manka R, Fleck E, Paetsch I (2007) Prognostic value of cardiac magnetic resonance stress tests: adenosine stress perfusion and dobutamine stress wall motion imaging. Circulation 115:1769–1776
Jensen JA, Mathorne J, Gravesen T, Stage B (1993) Deconvolution of in-vivo ultrasound B-mode images. Ultrason Imag 15(2):122–133
Kuhl CK, Schild HH (2000) Dynamic image interpretation of MRI of the breast. J Magn Reson Imaging 12(6):965–974
Lange K, Carson R (1984) EM reconstruction algorithms for emission and transmission tomography. J Comput Assist Tomogr 8:306–316
Liang ZP, Lauterbur PC (2000) Principles of magnetic resonance imaging: a signal processing perspective. IEEE press series on biomedical engineering. Wiley, New York
Mado K, Ishii Y, Mazaki T, Ushio M, Masuda H, Takayama T (2006) A case of bone metastasis of colon cancer that markedly responded to S-1/CPT-11 combination chemotherapy and became curable by resection. World J Surg Oncol 4:3
Malvehy J (2002) Follow-up of melanocytic skin lesions with digital total-body photography and digital dermoscopy: a two-step method. Clin Dermatol 20(3):297–304
McCollough CH (1997) X-ray production. Radiographics 17(4):967–984
McKetty MH (1998) X-ray attenuation. Radiographics 18(1):151–163
Mettler M, Guiberteau MJ (2005) Essentials of nuclear medicine imaging. Saunders, Maryland Heights
Mori S, van Zijl PCM (2002) Fiber tracking: principles and strategies—a technical review. NMR Biomed 5(7–8):468–480
Meijering EHW, Niessen WJ, Viergever MA (1999) Retrospective motion correction in digital subtraction angiography: a review. IEEE Trans Med Imaging 18(1):2–21
Ning R, Chen B, Yu R, Conover D, Tang X, Ning Y (2000) Flat panel detector-based cone-beam volume CT angiography imaging: system evaluation. IEEE Trans Med Imaging 19(9):949–963
Papanicolaou AC (1995) An introduction to magnetoencephalography with some applications. Brain Cogn 27(3):331–352
Pelizzari CA, Chen GTY, Spelbring DR, Weichselbaum RR, Chen CT (1989) Accurate three-dimensional registration of CT, PET, and/or MR images of the brain. J Comput Assist Tomogr 13(1):20–26
Pooley RA, McKinney JM, Miller DA (2001) Digital fluoroscopy. Radiographics 21(2):512–534
Prince JL, Links J (2005) Medical imaging signals and systems. Prentice Hall, New York
Robb RA, Sinak LJ, Hoffman EA, Kinsey JH, Harris LD, Ritman EL (1982) Dynamic volume imaging of moving organs. J Med Syst 6(6):539–554
Rogers A (2004) T cells cause lung damage in emphysema. PLoS Med 1(1):e25
Saine PJ, Tyler ME (2002) Ophthalmic photography: retinal photography, angiography, and electronic imaging, 2nd edn. Butterworth-Heinemann, Stoneham

Salibi N, Brown MA (1998) Clinical MR spectroscopy: first principles. Wiley, New York
Senda M, Kimura Y, Herscovitch P (2002) Brain imaging using PET. Academic Press, San Diego
Shcherbinin S, Celler A, Belhocine T, Vanderwerf R, Driedger A (2008) Accuracy of quantitative reconstructions in SPECT/CT imaging. Phys Med Biol 53(17):4595–4604
Szabo T (2004) Diagnostic ultrasound imaging: inside out. Academic press series in biomedical engineering
Török P, Kao FJ (2008) Optical imaging and microscopy. Techniques and advanced systems, Springer series in optical sciences
van Zuijlen PPM, Angeles AP, Kreis RW, Bos KE, Middelkoop E (2002) Scar assessment tools: implications for current research. Plast Reconstr Surg 109(3):1108–1122
Wagner RF, Insana MF, Brown DG (1985) Unified approach to the detection and classification of speckle texture in diagnostic ultrasound. Int Conf Speckle 556:146–152
Wang J, Blackburn TJ (2000) X-ray image intensifiers for fluoroscopy. Radiographics 20(5):1471–1477
Wu CM, Chen YC, Hsieh KS (1992) Texture features for classification of ultrasonic liver images. IEEE Trans Med Imaging 11(2):141–152

http://www.springer.com/978-1-4471-2750-5

Guide to Medical Image Analysis
Methods and Algorithms
Toennies, K.D.
2012, XX, 468 p., Hardcover
ISBN: 978-1-4471-2750-5